



Maximization of inertial waves focusing in linear and nonlinear regimes

A. Mohamed 

*Ecole Centrale de Lyon, CNRS, Université Claude Bernard Lyon 1, INSA Lyon,
LMFA, UMR5509, 69130, Ecully, France*

A. Delache *

*Ecole Centrale de Lyon, CNRS, Université Claude Bernard Lyon 1, INSA Lyon, LMFA,
UMR5509, 69130, Ecully, France
and Université Jean Monnet, 42100 Saint-Étienne, France*

F. S. Godefert 

*CNRS, Ecole Centrale de Lyon, INSA Lyon, Université Claude Bernard Lyon 1,
LMFA, UMR5509, 69130, Ecully, France*

J. Liu, M. Oberlack , and Y. Wang 

Fachgebiet Strömungsdynamik, TU Darmstadt, 64287 Darmstadt, Germany



(Received 20 September 2023; accepted 8 August 2024; published 13 September 2024)

We study the propagation of inertial waves (IW) generated by an axisymmetric torus oscillating at frequency ω_f in a rotating fluid. Inertial waves are emitted from the torus and propagate at an angle θ_f that depends on the ratio of the rotation frequency of the fluid to the forcing frequency of the torus. The waves focus in a neighborhood of the apex of the propagation cone. Using direct numerical simulations, we characterize the flow in this region, within a linear approximation or in the regime where nonlinear interactions between waves produce a turbulent patch. Forcing by the torus is modeled in two ways. The first model represents the effect of the oscillating torus as a local volume force in the form of a Dirac delta function, called the Dirac ring. The second approach aims at a more realistic three-dimensional model of a torus represented by a volume penalization technique. We observe the appearance of a mean flow composed of a central vortex produced by the nonlinear interaction of the IWs. We show that this phenomenon is in agreement with the theory of Davidson *et al.* [*J. Fluid Mech.* **557**, 135 (2006)] for a rotating fluid. Using Dirac ring forcing in the linear regime, we obtain the dependence on the propagation angle of the vertical kinetic energy at the focal point, which reaches a maximum for $\theta_f = 35^\circ$, in agreement with the linear theory developed by Liu *et al.* [*Phys. Fluids* **34**, 086601 (2022)]. A similar angle is observed in the 3D torus forcing case for both linear and nonlinear simulations: the angle $\theta_f = 30^\circ$ maximizes the vertical velocity and dissipation, attesting an optimal energy transfer from the oscillating source to the focal region. In the nonlinear regime, we obtain the detailed spectral distribution of the kinetic energy in the focal zone, and we develop a spatiotemporal analysis of the velocity field that shows a wide presence of IWs in the flow. Moreover, we identify triadic resonances of IWs that lead to the production of the turbulent patch and of a large-scale mode similar to the geostrophic mean flow.

DOI: [10.1103/PhysRevFluids.9.094605](https://doi.org/10.1103/PhysRevFluids.9.094605)

*Contact author: alexandre.delache@ec-lyon.fr

I. INTRODUCTION

Geophysical and astrophysical flows are often submitted to a buoyancy force induced by stable stratification and/or to Coriolis force, respectively, induced by rotation, respectively leading to the appearance of internal gravity waves (GWs), inertial waves (IW), or inertial gravity waves (IGWs) when stratification and rotation are both present. In the dynamics of liquid cores of planets [1] or Earth's equatorial atmosphere [2] IWs play an important role, whereas GWs are particularly present in the ocean even when coupled to large-scale motion due to rotation. In the ocean, the energy injected by the tides leads to internal GWs that propagate and dissipate through various mechanisms, such as wave breaking, that eventually produce 3D turbulence and enhance mixing [3]. In addition, these waves contribute to the transport of heat and dissolved greenhouse gases, which are important phenomena for climate modeling [4]. The conversion of tidal forces into internal waves occurs when tidal currents encounter the topography of the seafloor and emit internal GWs. Several of these waves can then interact with each other at remote distance of the topography and eventually produce a local zone of turbulence that geophysicists call *remote turbulence* [5].

Remote turbulence is the result of local conversion of energy due to wave transport and wave breaking occurring at remote topography. Energy exchanges between waves of different scales and local eddies can then concentrate turbulent energy to varying degrees. But geometry also plays an amplifying role when the rays of the waves are concentrated in a localized region called the focal zone. Such geometric effects can be due to a horizontal curvature of the topography, as confirmed by *in situ* measurements in an oceanic canyon [6], in a strait [7], or in an enclosed crater [8]. Several studies have investigated the focusing of conical waves generated by an oscillating sphere in an inviscid stratified fluid [9], by vertical oscillations of a horizontal disk in a stratified fluid [10], by a librating disk in an inertial wave context [11,12] or by periodic axial compression in a closed rotating cylinder of gas [13]. More complex shapes were also considered such as background topography in the form of a circular ring with a Gaussian cross section or an elliptical ring (both by [14]) or a horseshoe-shaped ring [15] under tidal forcing. In the case of circular ring with a Gaussian cross section, the amplification rate of the waves when focusing was obtained using linear theory [14].

The configuration of a ring with a Gaussian cross section can be geometrically idealized in a flow containing an oscillating torus-shaped solid ring, hence reproducing the focusing of waves at the apex of the propagation cone with an angle θ_f [Fig. 1(b)]. Many configurations are possible, from experiments with a single torus [16] to experiments with a wave generator containing multiple concentric tori which can be configured to focus the waves [17]. Several studies in stratified or rotating fluids have analyzed this torus configuration: numerical simulations and experiments of IWs by Duran-Matute *et al.* [18], experiments of GWs [16,19–21] and of IGW [20], analysis and linear theory of GWs [22], or linear theory of IWs [23]. Since GWs and IWs are both transverse waves with similar dispersion relations, their dynamics can be expected to be comparable, at least qualitatively. In particular for IWs waves in a rotating flow, if the axis of rotation is along the vertical direction z with the rotating rate Ω_z , the relation between frequency ω_{dr} and wave vector $\mathbf{k} = (k_x, k_y, k_z)$ of a propagating IW satisfy the following dispersion relation [24]:

$$\omega_{dr}(\theta) = \pm 2\Omega_z \sin \theta, \quad (1)$$

where $\theta(\mathbf{k})$ is the angle between \mathbf{k} and the horizontal plane, called the propagation angle, such that $\sin \theta(\mathbf{k}) = k_z/|\mathbf{k}|$ [see Fig. 1(a)]. For GWs, the dispersion relation is similar by replacing the sine dependence in θ by a cosine function, and the rotation rate by the stratification intensity parameter (Brunt-Väisälä frequency).

The structure of the waves emitted by an oscillating object changes depending on the presence of viscous effects. For instance, uni- and bimodality for the waves emitted by a sphere are discussed by Voisin *et al.* [25]. Large viscosity yields a unimodal form: the waves appear as a single wave beam with maximum wave amplitude in its center, and they form a single focusing region [16,19]. At low viscosity a bimodal form is observed, with each section of the torus generating two rays tangential

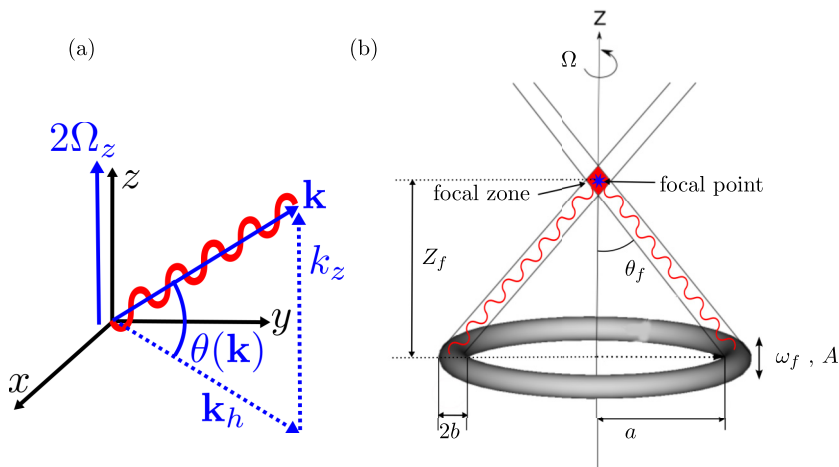


FIG. 1. (a) Illustration of a propagating inertial wave with wave vector \mathbf{k} and propagation angle $\theta(\mathbf{k})$. (b) Illustration of the conical focusing of IWs emitted by a torus vertically oscillating at frequency ω_f with amplitude A .

to its boundary that cannot merge into a single wave beam due to low viscous diffusion, so that they lead to four focusing regions [20]. In either unimodal or bimodal form, the conical structure of the wave beams for the torus configuration is geometrically confined.

In terms of dynamics, the flow motion is either in a regime of linear wave superposition or in a nonlinear regime of wave interactions with possible local overturning of the density in the stably stratified case [16], depending on the ratio between the amplitude of forced oscillations and the large radius of the torus, quantified by the Keulegan-Carpenter nondimensional number (see Sec. II B). For the linear regime of waves, based on the theoretical work available for an oscillating sphere [25] and for an oscillating torus [19], one finds a preferential propagation angle θ_p at which the growth of the fluid velocity amplitude in the focal region is maximal for GWs. For IWs in a rotating fluid, this preferential angle was found to depend on the parameters of the configuration when the local forcing is modeled as a Dirac ring [23]. At the angle θ_p , the maximum wave energy is transferred from torus oscillations to the vertical velocity in the focal zone, hence triggering a localized turbulent state when nonlinearities eventually kick in.

In the present work we use direct numerical simulations (DNS) to investigate the existence of an optimal propagation angle, in a configuration close to the theoretical approach assuming localized ring forcing, or by considering a full 3D model of the torus. A second question concerns the nonlinear wave regime, in which resonant triads are a mechanism of energy redistribution between waves at different scales, as experimentally demonstrated in a unimodal form [19] for GWs and in a bimodal form for GWs and IGWs (by the addition of rotation) [20]. In the review of Dauxois *et al.* [26] of the instability of an GW beam, two mechanisms lead to the energy exchange between different scales. The first is resonant triads between waves. The second is the generation of a mean flow from internal GW beams by a streaming instability due to nonlinear interactions of the oscillating wave beam with itself. Can similar mechanisms be observed for IWs focusing in a rotation flow such as resonant triads and generation of mean flow? Alternatively, is there an optimal propagation angle that amplifies the focusing to its maximum when varying the Rossby number and keeping all other flow parameters unchanged? Although this last question was discussed by Shmakova and Flór [19] for the stratification with GWs, it is still pending in the case of pure rotation with IWs.

In order to answer these questions, we use DNS of a vertically oscillating torus in a rotating fluid to reproduce the phenomenon of wave focusing at the apex of the wave propagation cone. We use

a systematic comparison between the linear and nonlinear DNS to contrast the two regimes when possible and to better highlight effects that are inherently nonlinear. In what follows, we first present the governing equations and the numerical framework in Sec. II B. In this section, we also expose the method used in DNS to model the forcing by the oscillations of a 3D circular torus or of an idealized ring of Dirac with negligible size. In Sec. III we highlight the bimodal form of our flow as well as the streaming-like instability that generates a mean flow observed by time averaging. In Sec. IV we evidence the presence of a propagation angle that maximizes the transfer of energy from the torus to the focal zone by computing both the vertical velocity and the kinetic energy dissipation. Finally, in Sec. V we show that the flow is largely dominated by the presence of IWs driven by resonant triads.

II. NUMERICAL SIMULATIONS

A. Configuration and governing equations

We consider a rotating fluid submitted to a vertical oscillation of a torus at frequency ω_f with amplitude A [Fig. 1(b)]. The torus largest radius is a and its smallest radius b . It sends energy in the form of an inertial wave cone, which concentrates energy with maximum at the apex of the cone. The dynamics of this rotating incompressible flow is described by the Navier-Stokes equations in a rotating frame [24] with adequate forcing terms:

$$\frac{\partial \mathbf{u}}{\partial t} + \boldsymbol{\omega} \times \mathbf{u} = -\frac{1}{\rho} \nabla p + \nu \nabla^2 \mathbf{u} - 2\boldsymbol{\Omega} \times \mathbf{u} + \mathbf{f}, \quad (2)$$

$$\nabla \cdot \mathbf{u} = 0, \quad (3)$$

where \mathbf{u} is the velocity field, $\boldsymbol{\omega} = \nabla \times \mathbf{u}$ is the vorticity, and p is a modified pressure that includes the centrifugal hydrostatic pressure. $\boldsymbol{\Omega} = [0, 0, \Omega_z]$ is the angular velocity with constant vertical rotation rate Ω_z , ρ is the density, and ν is the kinematic viscosity. The forcing term \mathbf{f} allows us to model the effect of the oscillating solid body with a forced frequency ω_f and amplitude A on the rotating fluid. For example, the classical Saint-Andrew's cross-shaped pattern of propagation of IWs is obtained by a pointwise Dirac forcing oscillating with a frequency ω_f , at a location \mathbf{x}_0 , with $\mathbf{f}(\mathbf{x}, t) = [0, 0, A \sin(\omega_f t) \delta(\mathbf{x} - \mathbf{x}_0)]$. In this paper, we study the oscillations of a 3D solid circular torus and of an idealized Dirac ring model. The latter simplifies the torus as a circular ring with negligible size, whose effect is represented by a local volume force in the momentum equation mathematically expressed as a Dirac delta function. This permits to retrieve the analytical results of Liu *et al.* [23] and to study the maximization of the focusing effect. This configuration of the Dirac ring is a guide to the exploration of parameters in the case of the 3D solid torus. Therefore, the two configurations are obtained numerically by using two kinds of body forces with different characteristics:

- (1) The vertically oscillating Dirac ring of radius a is modeled by a volume forcing as

$$\mathbf{f} = [0 \quad 0 \quad A_0 \sin(\omega_f t) H_0^{\text{DR}}(\mathbf{x})] \quad \text{with } H_0^{\text{DR}}(\mathbf{x}) = \delta(|\mathbf{x}| - a), \quad (4)$$

where A_0 is the inertial forcing amplitude.

- (2) The vertically oscillating 3D torus is modeled using a volume penalization method [27,28]. The penalization method was originally developed by Arquis *et al.* [29] to model the interface between a fluid and a porous medium with a ratio η between permeability and viscosity. In this method, the Navier-Stokes equation applies to both the porous medium and to the fluid, distinguished only by the forcing term that localizes the porous medium separately from the remaining fluid via a spatial mask function. Angot *et al.* [30] demonstrated that when $\eta \rightarrow 0$ the penalized region of the porous medium represents adequately a solid, and the global solution converges to a solution with no-slip boundary condition on the surface of the solid surrounded by fluid. The forcing term for

penalization is thus

$$\mathbf{f} = \frac{1}{\eta}(\mathbf{u} - \mathbf{u}_s)H^T(\mathbf{x}, t), \quad (5)$$

where $H^T(\mathbf{x}, t)$ is a mask function representing a torus-shaped solid body moving with vertical velocity $\dot{z}(t) = A\omega_f \sin(\omega_f t)$. Thus, $\mathbf{u}_s = [0, 0, \dot{z}(t)]$ is the velocity of a point on the torus due to vertical oscillation. The mask function is based on a solid torus body with largest radius a and smallest radius b as indicated in Fig. 1(b) and is defined at time $t = 0$ as

$$H_0^T(\mathbf{x}) = \begin{cases} 0 & \text{if } \mathbf{x} \notin \text{torus,} \\ 1 & \text{if } \mathbf{x} \in \text{torus.} \end{cases} \quad (6)$$

In Fourier space, we denote by $\hat{*}$ the Fourier coefficient for a wave number $\mathbf{k} = (k_x, k_y, k_z)$. The oscillating motion $z(t) = -A \cos(\omega_f t)$ of the solid can therefore be represented as the following phase change of the Fourier modes [27]:

$$\hat{H}^T(\mathbf{k}, t) = \hat{H}_0^T(\mathbf{k})e^{-ik_z z(t)}. \quad (7)$$

In both torus and Dirac ring, the regions oscillating at forcing frequency ω_f emit IWs propagating at an angle θ_f if ω_f satisfies the dispersion relation (1) of inertial wave, i.e., $\omega_f = \omega_{dr}(\theta_f)$. This leads to

$$\theta_f = \sin^{-1}(\omega_f/2\Omega_z). \quad (8)$$

Inertial waves propagating at an angle θ_f have no typical scale, so that their wavelength can range from large to small, in relation to the source size. Since the system is symmetric around the z axis and the waves form a cone of propagation, the main difference between the two configurations is that the Dirac ring produces a single focal point at height

$$Z_f = a \cot \theta_f, \quad (9)$$

whereas the 3D torus produces a wider focal zone [Fig. 1(b)] whose size is related to the torus radius b .

The difference in the injected power from the Dirac ring and the 3D torus, particularly in terms of their spectral breadth, is discussed in Appendix A.

B. Parameters and numerical setup

Equations (2) and (3) are solved using a standard pseudospectral method in a 2π -periodic cubic domain and using a spatial resolution of 512^3 points. In the 3D torus configuration with forcing (5), the penalization term is solved implicitly with $\eta = 10^{-6}$ s [28,31]. The oscillations close to the torus wall due to the discontinuity of the H_0^T function are filtered as in Kolomenskiy and Schneider ([27] Appendix A) with a Gaussian smoothing function $\hat{H}_0^T(\mathbf{k})e^{-C_s(k_x^2/N_x^2 + k_y^2/N_y^2 + k_z^2/N_z^2)}$ where $C_s = 16$ and N_x, N_y , and N_z the resolution in each direction. This gives a thicker mask function, and we note that Hester *et al.* [32] recently showed that it is possible to get second-order convergence with the penalization method using a carefully chosen adequate thickness of the mask function.

The flow produced by the oscillation of the 3D torus depends on several parameters: the geometry of the torus with radii (a, b) , the oscillation frequency ω_f and amplitude A , the rotation rate Ω_z , the kinematic viscosity ν . By using $T_0 = \omega_f^{-1}$, $L_0 = 2b$, $U_0 = A\omega_f$, ρ_0 and P_0 as characteristic time, length, velocity, density, and pressure, respectively, the nondimensional form of (2) without forcing is

$$\frac{1}{\text{Ke}} \frac{\partial \mathbf{u}}{\partial t} + \mathbf{u} \cdot \nabla \mathbf{u} = -E \nabla p + \frac{1}{\text{Re}} \nabla^2 \mathbf{u} - \frac{2}{\text{Ro}} \mathbf{e}_z \times \mathbf{u},$$

where $\text{Ke} = A/2b$ is the Keulegan-Carpenter number that represents the ratio of the forcing amplitude to the minor radius of the torus where $E = P_0/(\rho_0 U_0)$ is the Euler number, $\text{Ro} = A\omega_f/(\Omega_z 2b)$

TABLE I. Simulation parameters for the case of Dirac ring, labeled DR, for which only linear DNS are run, and for the 3D torus configuration, labeled T, for which linear and nonlinear DNS are run. For the DR DNS runs numbered 4 to 24, θ_f varies from 40° to 60° by increments $\Delta\theta_f = 1^\circ$. The table shows the following values for DR and T configurations: the frequency of the fastest IW is $2\Omega_z$, the forcing frequency is $\omega_f = 5$ or $\omega_f = 1.256$, and the corresponding respective Rossby numbers are $\text{Ro} = \omega_f A / (a\Omega_z)$ for DR and $\text{Ro} = \omega_f A / (2b\Omega_z)$ for T. The frequency $2\Omega_z$ must be compared with the maximum pulsation $\omega_{\max} = 2\pi / \Delta t$ and minimum one $\omega_{\min} = 2\pi / T$ solved in the 4D Fourier transform for which the time series is characterized by its period $T = N\Delta t$, number of points N , and interval Δt (same parameters as the DNS time discretization). $N = 2000$, $\Delta t = 0.025$ for the T configuration, and $N = 500$, $\Delta t = 0.05$ for the DR configuration.

DR DNS	1	2	3	4	5	...	23	24	25	
$2\Omega_z$	5.077	5.32	5.77	6.52	6.62	...	9.7	10	14.61	
θ_f	80°	70°	60°	50°	49°	...	31°	30°	20°	
$\text{Ro}(\times 10^{-2})$	1.96	1.88	1.73	1.53	1.51	...	1.03	1	0.68	
ω_{\min}	0.25	0.25	0.25	0.25	0.25	...	0.25	0.25	0.25	
ω_{\max}	125	125	125	125	125	...	125	125	125	
T DNS	1	2	3	4	5	6	7	8	9	10
$2\Omega_z$	1.53	1.77	1.99	2.08	2.19	2.3	2.37	2.51	2.97	3.67
θ_f	55°	45°	39°	37°	35°	33°	32°	30°	25°	20°
$\text{Ro}(\times 10^{-2})$	1.37	1.18	1.05	1	0.96	0.91	0.88	0.83	0.7	0.57
ω_{\min}	0.126	0.126	0.126	0.126	0.126	0.126	0.126	0.126	0.126	0.126
ω_{\max}	251	251	251	251	251	251	251	251	251	251

is the Rossby number, and $\text{Re} = A\omega_f 2b/\nu$ is the Reynolds number. Classically, the reference pressure P_0 is not known and the default choice is $E = 1$. In that case, Ke , Re , and Ro characterize the flow. In a similar torus configuration in a stratified fluid, one can introduce the Stokes number $\text{St} = \text{Re}/\text{Ke} = \omega_f b^2/\nu$ to study the linear waves [16].

For Dirac ring forcing, the nondimensional numbers are obtained by changing $2b$ into a and A into A_0/ω_f^2 . In this study, we focus on the search for the optimal propagation angle θ_f that maximizes the energy focusing of the IWs, so that we restrict the parameter space by keeping constant the geometrical parameters of the 3D torus ($a = 0.848$, $b = 0.0942$) and of the Dirac ring ($a = 1$). With these values, the focal point remains in the domain for all the forcing angles considered in our simulations in a cube of vertex length 2π .

In addition, when exploring the angle dependence of the energy-focusing efficiency with θ_f , we keep constant the three parameters $\text{Re} \gg 1$, $\text{Ke} \ll 1$, and $\text{St} \gg 1$ by keeping constant ν , A , and ω_f . We vary only the rotation rate Ω_z while ensuring $\text{Ro} \ll 1$. Note that IWs appear at low Reynolds and low Rossby numbers, whereas in the regime of high Reynolds and low Rossby numbers, wave-turbulence interactions are expected to occur [33].

Two sets of direct numerical simulations have been run for the two configurations. For the Dirac ring configuration, we run only linear simulations obtained by setting $\boldsymbol{\omega} \times \mathbf{u} = \mathbf{0}$ in Eq. (2), for comparison with the analytical results of Liu *et al.* [23]. We choose $\Delta t = 0.05$, $\nu = 10^{-4}$, $A_0 = 0.01$, $\omega_f = 5$ so that $\text{Re} = 100$, $\text{Ke} = 0.0004 \ll 1$, and $\text{St} = 50\,000 \gg 1$. Twenty-five linear simulations use propagation angles from $\theta_f = 20^\circ$ to 80° adjusted by varying the rotation rate in the range $2\Omega_z = 5.077$ to 14.61 ; therefore $\text{Ro} \ll 1$ varies from 0.0038 to 0.00136 (see Table I). A tentative nonlinear DNS shows that most of the energy sent into the fluid feeds eddies that are close to the Dirac ring and not in the focal point, so with little influence in the focal region.

For the 3D torus configuration, the 10 simulations correspond to parameters detailed in Table I. They consist of a first linear simulation (again with $\boldsymbol{\omega} \times \mathbf{u} = \mathbf{0}$) run for a sufficiently long time so that the wave network has time to establish in the geometrical domain. The network is a side effect of the periodic boundary conditions, but similar reflections exist in physical experiments in containers

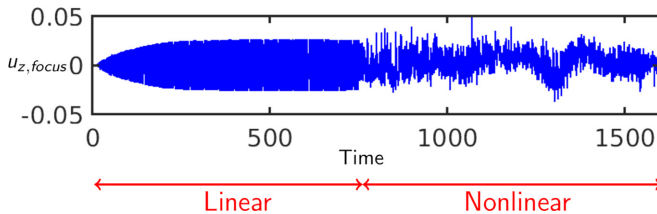


FIG. 2. Time series of vertical velocity $u_{z,\text{focus}}$ at the focal point Z_f in the case $\theta_f = 33^\circ$ from our DNS in the torus configuration.

with plane walls. A sponge zone technique [34] could be implemented numerically to absorb waves, but with a high numerical cost due to the enlargement of the domain, an increase of dissipation due to the buffer zone and small wave reflection. As far as we know, laboratory experiments are obtained either in the presence of rigid walls or in the presence of free interfaces (water surface). We also tested the effect of a rigid horizontal wall using the penalization method on our results. It shows that dissipation and energy in the bulk flow are twice as large in the presence of the wall than with periodic conditions. However, the concentration in the focal zone (the ratio of the focal zone to the total) is about the same for energy and dissipation. In addition, these linear simulations can be compared to the linear simulations in the configuration of the Dirac ring. Starting with this linear flow state we then pursue fully nonlinear DNS with $\boldsymbol{\omega} \times \mathbf{u} \neq \mathbf{0}$, to study the nonlinear focusing of the IWs that produces local turbulence in the focal region. For the 10 DNS, we choose $\Delta t = 0.025$, $\nu = 10^{-5}$, $A = 0.0157$, $\omega_f = 1.256$ so that $\text{Re} = 372$, $\text{Ke} = 0.083 \ll 1$, and $\text{St} = 1115 \gg 1$. The simulations differ by their forcing angles θ_f from 20° to 55° adjusted by varying $2\Omega_z \in [1.53, 3.67]$ and therefore $\text{Ro} \in [0.057, 0.137]$, again maintaining $\text{Ro} \ll 1$ (see Table I). Figure 2 shows a time series of the vertical velocity including the linear and nonlinear phases of the simulation. For the majority of DNS, convergence in the linear phase requires a duration of about $150T_{\Omega_z}$ where $T_{\Omega_z} = 2\pi/\Omega_z$ is the rotation period of the fluid.

Although we keep Ke and Re constant and vary only Ro in our simulations, one can also discuss the role of the Ekman number $\text{Ek} = \text{Ro}/\text{Re} = \nu/(\Omega_z b)$ in relation with the presence of boundary layers on the torus. The wave beams originate from the oscillating torus due to the oscillating Ekman boundary layers that break at critical latitudes into IWs. One can estimate the transport velocities of the shear layer and therefore of the waves, which vary between $\text{Ek}^{1/6}$ and $\text{Ek}^{3/10}$ (see Fig. 1 in [35]). In our DNS, this means that velocities injected in waves vary from about $\sim 15\%$ to $\sim 30\%$ between low and high Ro .

Nevertheless, the viscous spreading of the wave beam (size and amplitude) and the associated decay of the velocity and vorticity envelopes depend on the distance x from the source and on the viscous length $l = [\nu/(2\Omega_z \sin \theta_f)]^{1/2}$ [36,37]. Hence, by varying only Ω_z in the DNS and keeping ω_f constant, $l \simeq 2.8 \times 10^{-3}$ remains constant, and all the beams undergo the same decay and arrive in the focal zone with the same energy loss whatever the Ro . This would not be the case if Ω_z were kept constant and ω_f varied in order to keep Ek constant and also the wave velocity. With the chosen values of ω_f and θ_f from 55° to 20° , l variation is 55%. Our choice is to retain the same beam characteristics with a slight reduction in energy.

III. ORGANIZATION OF THE FLOW

A. Focal zone and wave structure

We analyze here the organization of the flow for the 3D torus configuration for both the linear stage and the following nonlinear regime.

Due to the vertical axial symmetry of the torus, the velocity field in the linear case is expected to be also symmetric, since no symmetry-breaking mechanism is present. Therefore, in this regime, the superposition of all the propagating IWs results in zero horizontal velocity and maximal vertical

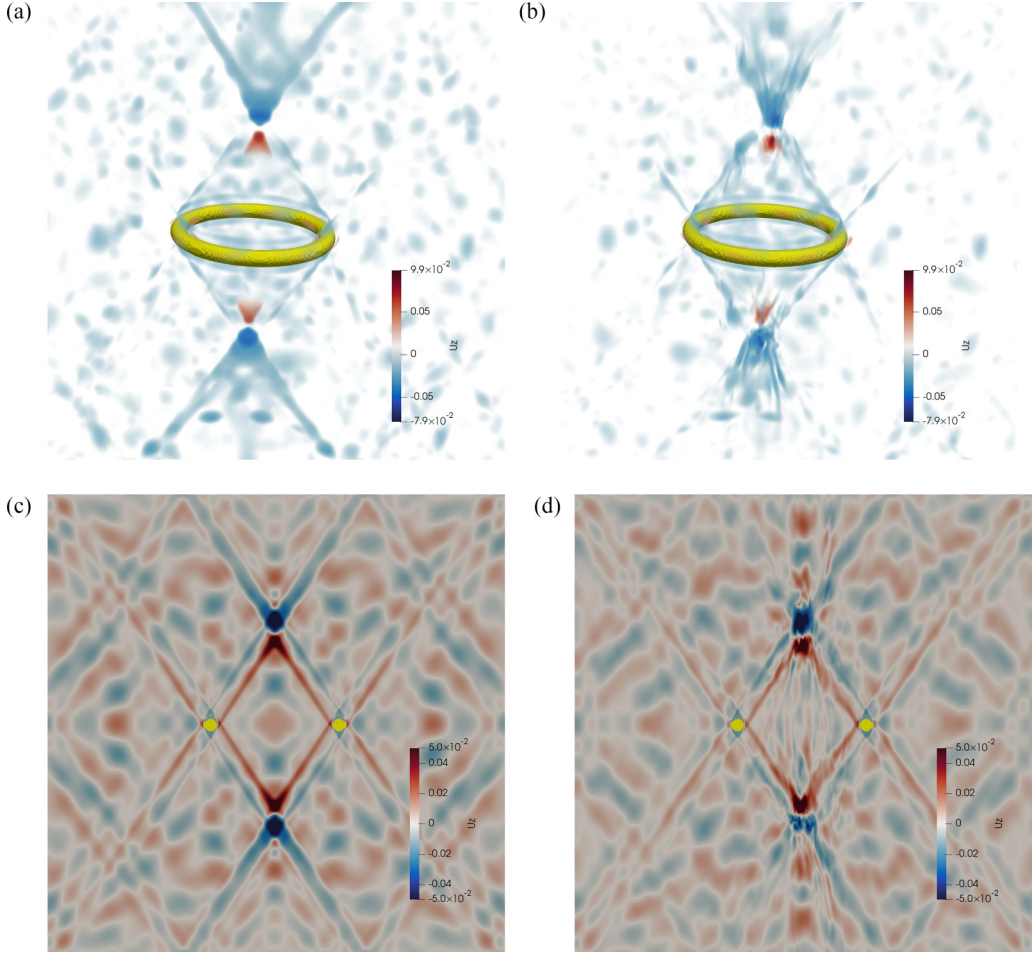


FIG. 3. Visualization of the instantaneous vertical velocity u_z at a given time t from a numerical simulation with $\theta_f = 33^\circ$ with oscillating 3D torus (shown in yellow). Linear simulation results with (a) 3D volume rendering (values of u_z close to 0 are transparent) and (c) in a 2D vertical (x, z) plane. Nonlinear simulation (b) for 3D volume rendering and (d) in a 2D vertical plane.

velocity on the central axis of the focal zone. This is observed in Fig. 3(a) for the 3D distribution around the torus and Fig. 3(c) for the 2D vertical plane cut distribution of the instantaneous vertical velocity field from the linear simulation at propagation angle $\theta_f = 33^\circ$. Moreover, the IWs have the form of a bimodal beam since each section of the torus generates two rays tangential to the torus boundary. Figures 3(a) and 3(b) also show that these rays do not merge into a single wave beam by diffusion as in other cases [20] because the Stokes number $St = 1115 \gg 1$ is too large for this to occur, as discussed in the Introduction.

Figures 3(b) and 3(d) show the vertical velocity distributions for the nonlinear regime. They reveal that the initial concentration of vertical velocity in the focal zone due to linear superposition of waves eventually turns into nonlinear interactions that create a localized turbulent state. The 3D visualization of Fig. 3(b) shows that the overall organization of the flow has a conical shape consistent with the cylindrical symmetry, and the maximum velocity is located in the focal zone. The vertical section of Fig. 3(d) shows details of the flow organization inside the cone, with two main features: (i) secondary IWs emerging from the focal region and propagating at an intermediate

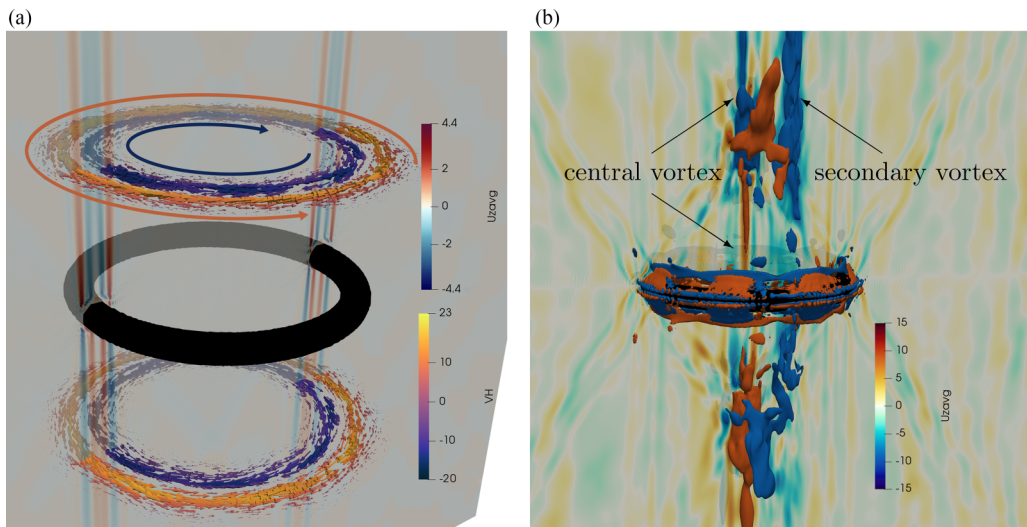


FIG. 4. Visualization of the averaged velocity from DNS at $\theta_f = 33^\circ$ (the 3D torus is in black). (a) 3D visualization of averaged vertical velocity \bar{u}_z (blue to red) and velocity vector in two horizontal cuts colored by the average horizontal velocity u_h^{avg} (black to yellow) in the linear simulation. (b) 3D visualization of vertical average velocity \bar{u}_z (blue to red) in a vertical cut and two isosurfaces of $\bar{u}_z = \pm 9$ (chosen at 12.1% of the maximum of u_z) in the nonlinear simulation.

propagation angle closer to vertical than the incoming waves and (ii) a vertical structure reminiscent of Taylor-like columns in rotating flows. Overall, the nonlinear flow is slightly different but not too far from the linear wave propagation flow. The corresponding regime is therefore that of weak wave turbulence, with the addition of a vertical mode that will be further discussed in the next section, Sec. III B.

B. Main averaged flow

The main averaged flow is obtained by time averaging the velocity field over N times, as

$$\bar{\mathbf{u}}(\mathbf{x}) = \frac{1}{N} \sum_{i=1}^N \mathbf{u}(\mathbf{x}, t_i). \quad (10)$$

The main averaged flows in the linear and nonlinear regimes are shown in Fig. 4. In the linear DNS [Fig. 4(a)], IWs are linearly superimposed and disappear when averaged, even in the focal zone. All that remains is the main flow that contains two large-scale rotors in the form of two cylinders turning clockwise and counterclockwise and elongated in the vertical direction (corresponding to a small vertical wave number $k_z \simeq 0$) with a radius of the order of the large torus radius. Indeed, under the assumption of linearity and stationary, the linear Taylor-Proudman theorem [38] can be applied so that $\partial u_z / \partial z = 0$. The flow is therefore invariant along the z axis and is 2D with two (2D2C) or three velocity components (2D3C). The vertical displacement imposed by the torus is therefore reflected throughout the fluid column above the torus to ensure that $\partial u_z / \partial z = 0$. One concludes that the large scale observed in linear simulation appears as a classical Taylor column triggered by the displacement of a solid body in a rotating fluid.

An important question concerns the persistence of such Taylor columns in turbulent regimes. Large structures identified to geostrophic modes [39] are observed in rotating flows in experiments by Brunet *et al.* [40] where the flow is forced by oscillating cylinders, by Boury *et al.* [41] where a trapezoidal domain is forced by a wave generator, or in simulations by Le Reun *et al.* [42] where

the flow is excited by the elliptical instability. Geostrophic modes are similar in shape to Taylor columns but with richer dynamics.

In our nonlinear simulations, the main averaged flow observed in Fig. 4(b) is rather different. First, we observe that the Taylor columns remain but are significantly weaker than a central and secondary vortex that appears along the vertical axis of the torus. This vortex appears to originate from the focal zone and to extend towards the central point of the torus. It was already observed in experiments and DNS by Duran-Matute *et al.* [18]. Second, as will be quantitatively confirmed in Sec. V, the flow is dominated by waves, so that we expect that the central vortex energy comes from a conversion of wave energy due to nonlinear mechanisms.

In the context of rotating fluids, the theory of Davidson *et al.* [43], confirmed by the numerical experiments of Ranjan and Davidson [44], is the one that comes closest to our configuration among the few theories that explain the emergence of columnar vortices. This theory is based on the linear emission of IWs by a localized patch or "blob" of turbulence produced by nonlinear interactions. Inertial waves emitted from this blob propagate at faster group velocity for low frequency $\omega \simeq 0$ in the vertical direction ($\mathbf{k} \perp \boldsymbol{\Omega}$) than for any higher frequency in other directions. They impose themselves on the flow, giving rise to columnar features. Nonlinear effects on IWs acting over longer periods of time are supposed to develop and maintain this structure. In the present nonlinear simulations, the focal zone can be considered as a blob resulting from nonlinear interactions of IWs, unlike the focal zone in the linear case which is a mere linear superposition of IWs. Helicity is in the following used as a diagnostic to confirm that these structures are formed by IWs, as proposed in [44], since IWs with negative helicity propagate upwards (relative to the axis of rotation), while waves with positive helicity propagate downwards.

In order to confirm this, we plot in Fig. 5 the distribution of the vertical helicity $\mathcal{H}_z = u_z \omega_z$ of the instantaneous flow and helicity $\mathcal{H}_z^{\text{avg}} = u_z^{\text{avg}} \omega_z^{\text{avg}}$ of the mean averaged flow in a vertical plane. The helicity for the instantaneous and averaged fields obtained by linear simulations is shown in Figs. 5(a) and 5(c), respectively. The distribution of instantaneous field helicity is directly related to the propagation of the IWs, and is concentrated along the rays of propagation of the waves and in the focal region. When averaged over several dozen periods, the (periodic) wave pattern disappears from the distribution of the flow helicity, while the Taylor column remains, having negative helicity above, and positive helicity below the ring. The flow has zero background helicity, and overall, the net helicity, obtained by summing over the domain, is zero.

Helicity in the nonlinear regime is shown in Figs. 5(b) and 5(d) for the instantaneous and averaged fields, respectively. The distribution of the instantaneous field reminds is of the linear case from the presence of the waves' propagation pattern. However, the nonlinear interactions produce secondary waves emitted from the focal region, as well as a vertical mode in the vicinity of the axis of symmetry. We also note that the helicity amplitude is very similar in linear and nonlinear simulations, and this is true as well for the averaged flow helicity. The latter is plotted for the nonlinear DNS in Fig. 5(d). By definition, averaging a field means filtering the low frequencies $\omega \simeq 0$ in the linear and nonlinear cases. Inertial waves such as $\omega \simeq 0$ are then filtered out. In contrast to the linear case, the wave pattern of primary propagating waves emitted by the torus is still present. Background helicity far from the center region is small, if not zero.

Most striking is that the averaged helicity distribution (for the nonlinear DNS) reveals a maximum of concentration in and around the focal region, that extends throughout the vertical extent of the fluid domain. The average shown in Fig. 5(d) shows that the helicity $\mathcal{H}_z^{\text{avg}}$ in the central vortex is of sign opposite to the helicity in the wave cones, which seems to be a signature of the evolution of a turbulent cloud under rotation. The development of the central vortex observed here is in agreement with the description by Davidson *et al.* [43] and Ranjan and Davidson [44] for grid turbulence and DNS of homogeneous turbulence.

For the sake of a critical discussion of various theories, one can mention Greenspan's [39] theorem that prohibits the formation of geostrophic modes (close to the columnar vortex) by an exact resonant triadic mechanism in a rotating fluid. Two other mechanisms can bypass Greenspan's theorem and transfer energy from wave interaction to columnar vortex such as quasiresonant triadic

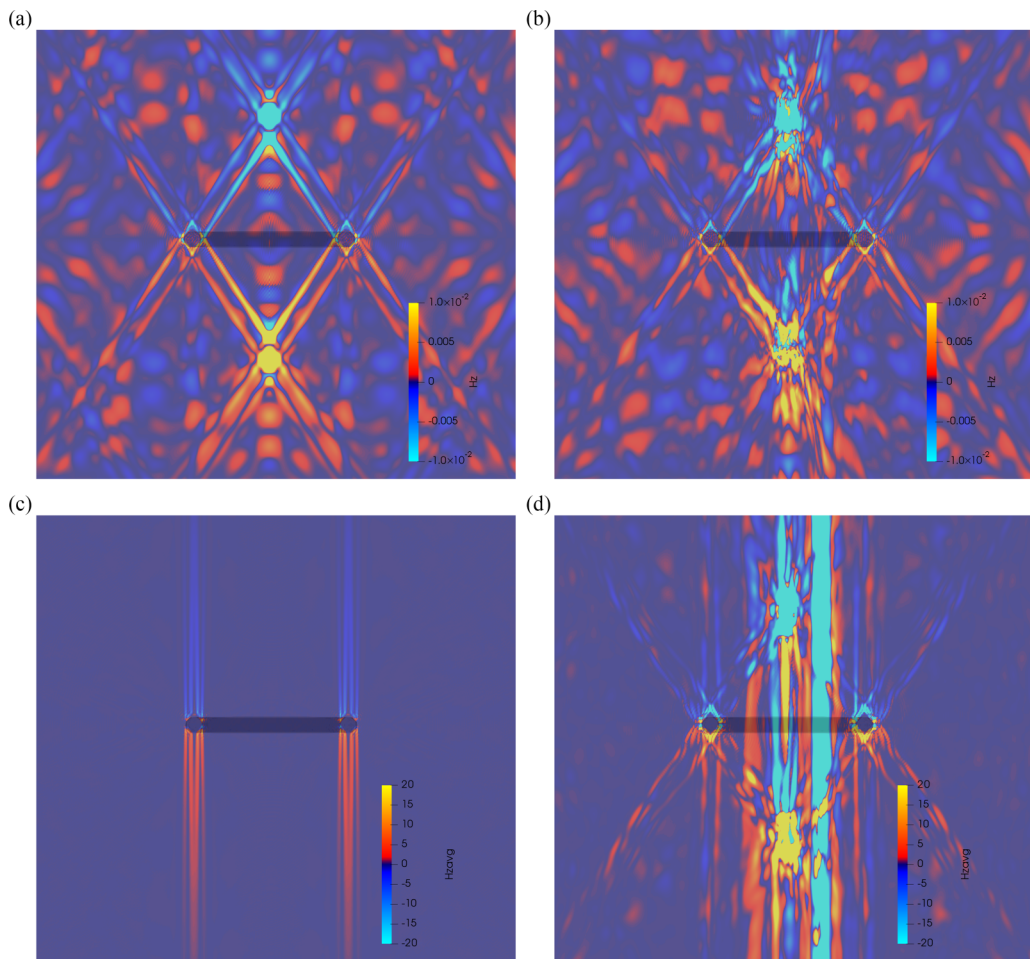


FIG. 5. Distribution of vertical helicity in a vertical plane containing the axis of symmetry, for $\theta_f = 33^\circ$ in simulation for the 3D torus. Colors: red for positive helicity and blue for negative helicity. (a) Linear and (b) nonlinear data for the instantaneous vertical helicity \mathcal{H}_z ; (c) linear and (d) nonlinear data for the averaged vertical helicity $\mathcal{H}_z^{\text{avg}}$. The shadow of the torus is shown in black. The domain shown is only five-sixths of the size of the calculation box, which is 2π .

interactions [45,46] and quartet interactions [40,47]. In fully developed rotating turbulence, it was shown that the geostrophic mode is largely dominated by wave/wave interactions [48] without identification of the precise mechanisms. It is not easy to isolate such wave/wave interactions in wave turbulence or in fully developed turbulence, and all the more in our geometry where turbulence is confined and concentrated within a small region. Other theories may explain the generation of a main flow such as streaming instability observed in experiments of stratified fluid [26,49], but it is yet to be adapted to rotating fluids. A possible hint is the role of helicity, which we have used as a diagnostic tool in the framework of Davidson's theory, but helicity plays also an important role in the transition from 3D to 2D turbulence without the presence of waves [50–52]. In this transition, the level of helicity in spatial triads plays an important role (for further reading see [50] and [51]).

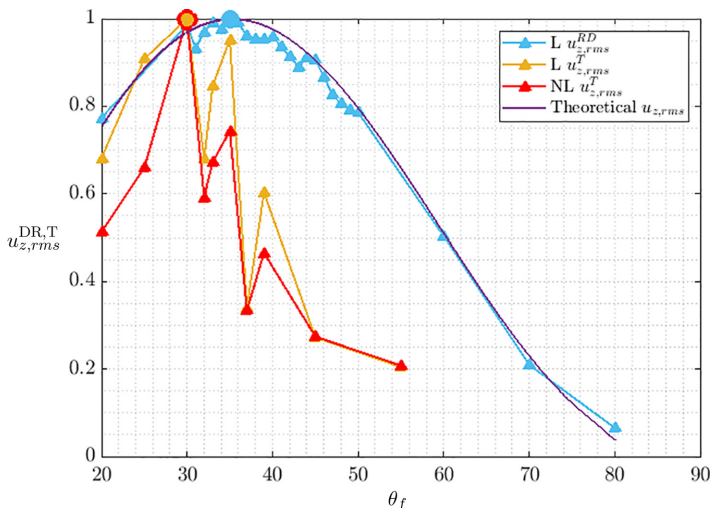


FIG. 6. RMS of vertical velocity u_z in the focal zone as a function of the propagation angle θ_f : solid purple curve without symbols for the theoretical result of Dirac ring configuration adapted from Liu *et al.* [23]; cyan triangles for the linear numerical simulations for the ring of Dirac configuration (DR index); orange triangles for the 3D torus configuration (T index) in the linear simulation; and red symbols for the nonlinear simulation. The large circles in blue and red indicate the maximum of each curve.

IV. MAXIMUM ENERGY TRANSFER IN THE FOCAL ZONE

In order to characterize the efficiency of the energy input by the forcing into the focal region, we investigate hereafter the evolution with θ_f of the root mean square (rms) vertical velocity in this region—which amounts to evaluating the vertical kinetic energy—and of the kinetic energy dissipation.

A. Vertical velocity in the focal zone

Due to axisymmetry, the linear superposition of waves at the focal point results in a concentration of vertical velocity and zero horizontal velocity. We investigate this property and compare it to the nonlinear regime obtained by DNS. For that, we start by defining a neighborhood of the focal point in which we quantify the energy coming from the oscillating torus that feeds the vertical velocity. Both the 3D torus and the ring of Dirac configurations are considered in the numerical simulations.

For the ring of Dirac configuration, we compute the vertical velocity u_z in a small cube around the theoretical position of the focal point at altitude Z_f computed in Eq. (9). This cube is defined by the four grid cells surrounding the focal point and is denoted C^{DR} . For the 3D torus configuration, the focal zone is spread out, and we define it as the points inside a sphere C^{T} of radius $R = 0.5$ with a center at height Z_f . The location of C^{T} is shown in Fig. 7. For the two configurations, we compute the rms vertical velocity averaged over N times t_i and in space over the cube C^{DR} or the sphere C^{T} :

$$u_{z,\text{rms}}^{\text{DR,T}} = \sqrt{\frac{1}{NN^{\text{DR,T}}} \sum_{j=1}^{N^{\text{DR,T}}} \sum_{i=1}^N [(u_z(\mathbf{x}_j, t_i) - \bar{u}_z(\mathbf{x}_j))]^2}, \quad (11)$$

where $\bar{u}_z(\mathbf{x}_j)$ is the time average of u_z at point \mathbf{x}_j in C^{DR} or C^{T} and $N^{\text{DR,T}}$ is the number of points within C^{DR} or C^{T} .

We characterize the transfer of energy to the vertical velocity by computing the velocity amplitude and its dependence on θ_f . Figure 6 shows the dependence of $u_{z,\text{rms}}^{\text{DR}}$ and $u_{z,\text{rms}}^{\text{T}}$ on θ_f . For the Dirac ring case, the linear numerical simulation result matches closely the theoretical result

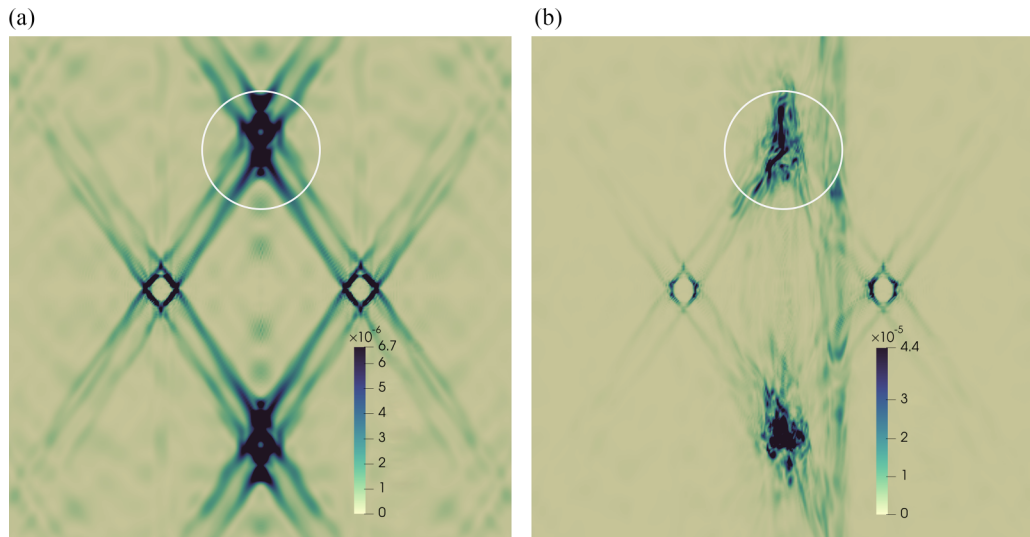


FIG. 7. Distribution of the instantaneous dissipation field $\varepsilon(\mathbf{x}, t)$ in a vertical azimuthal plane, for the torus configuration, at $\theta_f = 33^\circ$. (a) Linear simulation; (b) nonlinear simulation. The white circle delimitates the focal zone C^T .

derived from Liu *et al.* [23]. For the simulation and the theoretical results, the maximum vertical velocity in the focal zone is observed at $\theta_{\text{DNS}}^{\text{DR}} \simeq 35^\circ$. For the 3D torus configuration, we observe larger oscillations of the curves $u_{z,\text{rms}}(\theta_f)$ than in the Dirac ring case. We attribute this to the higher sensitivity of the forced wave packets to the topology of the flow in the vicinity of the torus. Nonetheless, in Fig. 6 for the 3D torus configuration (obtained with nonlinear DNS), the amplitude curve clearly indicates a maximum at $\theta_{\text{DNS}}^{\text{T}} \simeq 30^\circ$, i.e., close to the value for the Dirac ring case.

These data can be compared with those obtained in the literature for stratified fluids in similar forced propagation of internal waves. The latter's dispersion relation corresponds to propagation angles $\theta_{\text{GW}} = \pm N \cos^{-1}(\omega_f/N)$, where N is the Brunt-Väisälä frequency (the stronger the stratification, the larger N), differing only by the cosine function instead of a sine in the dispersion relation of rotating fluids [Eq. (8)]. Transposing our results, we therefore expect $\theta_{\text{GW}} = 90^\circ - \theta_{\text{IW}} \simeq 60^\circ$ in the case of stratification, close to the preferential angle $\theta_{\text{GW}} \simeq 55^\circ$ observed by Maffioli *et al.* [53] in DNS of stratified turbulence mixing GWs, eddies, and large-scale structures, also in good agreement with the linear theory that maximizes the horizontal energy flux of GWs found by Maffioli *et al.* [53]. It disagrees, however, with other results by Dohan and Sutherland [54] ($\theta_{\text{GW}} \simeq 35^\circ$ from linear theory maximizing the GW vertical energy), by Shmakova and Flór [19] ($\theta_{\text{GW}} = 35^\circ$), or by Voisin *et al.* [25] (analytical theory for a sphere or a cylinder). Note that the shape of the oscillating object as well as the different body force (gravity, Coriolis) could be responsible for the observed differences.

B. Dissipation in the focal zone

The energy sent by the torus and spatially propagated by the IWs is mainly dissipated in the focal zone. We compute the dissipation rate field in the fluid domain as $\varepsilon(\mathbf{x}, t) = \nu[\nabla\mathbf{u}(\mathbf{x}, t)]^2$ and plot its distribution in an azimuthal vertical plane in Figs. 7(a) and 7(b) for the linear and nonlinear simulations, respectively, with $\theta_f = 33^\circ$. The strong concentration of dissipation in the focal zone C^T is clear, but the dissipation is concentrated in structures smaller in the nonlinear simulation than in the linear one, since the focal region appears as a turbulent patch. For the nonlinear simulation [Fig. 7(b)], the bottom focal zone exhibits a somehow more homogeneous concentration of dissipation than the top focal region. This is due only to the specific choice of azimuthal plane, which cuts through vertically elongated structures that rotate around the axis of

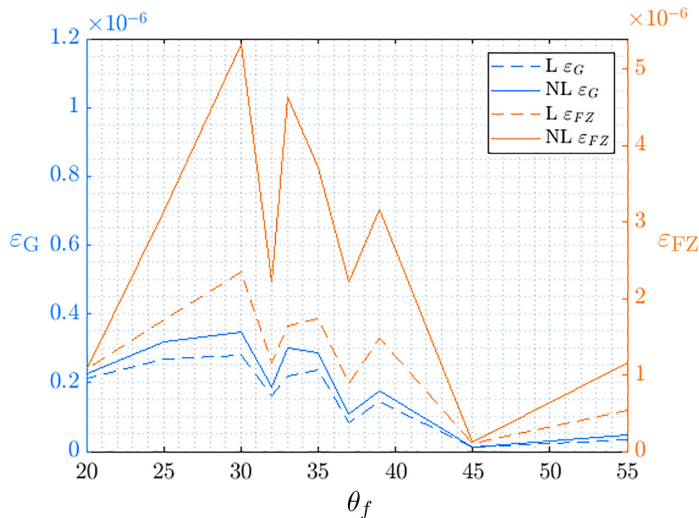


FIG. 8. Averaged dissipation rates ε_G in the whole fluid domain (blue curves) and ε_{FZ} in the focal zone (red curves), by numerical simulations for the 3D torus configuration. Solid lines for nonlinear simulation and dashed lines for the linear simulation, respectively, noted NL and L.

symmetry and can be captured differently depending on their azimuthal location. In order to quantify the concentration of dissipation, we define a space- and time-averaged dissipation rate by grid point in a volume V as

$$\bar{\varepsilon} = \frac{1}{N(V)} \sum_{j=1}^{N(V)} \sum_{i=1}^N \varepsilon(\mathbf{x}_j, t_i), \quad (12)$$

where $N(V)$ is the number of grid points in V , $\mathbf{x}_j \in V$ and N is the number of times for averaging. We compute the dissipation rate in the focal region ε_{FZ} by applying the average (12) to the focal zone with $V = C^T$. Moreover, we compute the global dissipation in the whole domain ε_G by applying (12) to the global fluid volume. We compare the two dissipation rates in Fig. 8 for different values of θ_f for linear and nonlinear simulations of the flow forced by the torus. As expected, more energy is dissipated in nonlinear simulations than in linear ones, and the concentration of energy in the focal region ε_{FZ} in the nonlinear simulation is almost 10 times larger than ε_G . In other words, with the same oscillation (same frequency ω_f and same amplitude A), there is more power sent by the torus in the focal zone in the nonlinear case than in the linear case. The maximum dissipation is reached for $\theta_{\text{DNS}}^T \simeq 30^\circ$, which is consistent with the peak vertical energy observed at this angle in Sec. IV A.

Oscillations are observed on the rms vertical velocity (Fig. 6) and on the dissipation rate (Fig. 8) for linear and nonlinear simulations. They reflect a variation of forcing in terms of available IWs: in a confined domain, multiple wave reflections superimpose different waves, creating stationary waves, also called inertial modes. This phenomenon was also observed experimentally by Boury *et al.* [55], and we discuss it further in Appendix B.

V. LINEAR AND NONLINEAR REGIMES FOR WAVES

A. Spatiotemporal analysis of flow and harmonic forcing

We focus here on the 3D torus configuration with the propagation angle $\theta_f = 33^\circ$ that maximizes vertical velocity and dissipation, as described in Sec. IV. We analyze the spatiotemporal spectral content of the flow to quantify the injected energy and identify the resulting waves that are produced. The presence of inertial wave propagation is attested by the verification of the dispersion relation

(1) applied to a 3D wave vector \mathbf{k} and a frequency ω . We thus carry out a 4D space-time Fourier transform of the velocity field $\mathbf{u}(\mathbf{x}, t)$ in our simulation data to obtain the transformed spectral field $\tilde{\mathbf{u}}(\mathbf{k}, \omega)$.

This kind of analysis was used by Yarom and Sharon [56] in experimental data of rotating turbulence and extended to DNS of stratified turbulence by Lam *et al.* [57]. We apply the 4D transformation $(\mathbf{x}, t) \rightarrow (\mathbf{k}, \omega)$ to fields of DNS in spectral Fourier space $\hat{\mathbf{u}}(\mathbf{k}, t)$, which are stored every one or two time steps depending on the case. In total, we use 1000 fields with a resolution of 512^3 points for the three velocity components. We then compute a temporal FFT with a Hann window to obtain $\tilde{\mathbf{u}}(\mathbf{k}, \omega)$. This completes the full 4D FFT transform. Compared to other methods—data reduction for a 2D analysis as done in experiments by Yarom and Sharon [56] and Campagne *et al.* [58], and in simulations by Clark Di Leoni *et al.* [59], or by using statistical homogeneity assumptions in Maffioli *et al.* [53]—our method requires larger memory storage and computational time, but with an evident gain of accuracy since a full detailed 3D analysis is permitted. Although the homogeneity assumption seems to be available in fully turbulent flows, it is not applicable in our linear simulations for the reason that the phase correlation of velocity modes is not random (see the Appendix in Maffioli *et al.* [53] for a detailed discussion about this assumption and a comparison with FFT4D).

We apply the 4D space-time analysis to obtain the fields $\tilde{\mathbf{u}}^L(\mathbf{k}, \omega)$ of the 10 linear DNS, and the fields $\tilde{\mathbf{u}}^{NL}(\mathbf{k}, \omega)$ of the 10 nonlinear ones. In Table I we report the minimum and maximum time frequencies ω_{\min} and ω_{\max} available in each case. Using these fields, we can successively compute the space-time spectrum of the kinetic energy density $E^{L,NL}(k_0, \omega)$ at scale k_0 and frequency ω , the temporal spectrum $E^{L,NL}(\omega)$ at frequency ω , the spatial spectrum $E^{L,NL}(k_0)$ at scale k_0 , and the total energy $E_{\text{tot}}^{L,NL}$ as

$$E^{L,NL}(k_0, \omega) = \sum_{k_0-0.5 \leq |\mathbf{k}| < k_0+0.5} |\tilde{\mathbf{u}}^{L,NL}(\mathbf{k}, \omega)|^2, \quad (13)$$

$$E^{L,NL}(\omega) = \sum_{k_0} E^{L,NL}(k_0, \omega), \quad (14)$$

$$E^{L,NL}(k_0) = \sum_{\omega} E^{L,NL}(k_0, \omega), \quad (15)$$

$$E_{\text{tot}}^{L,NL} = \sum_{k_0, \omega} E^{L,NL}(k_0, \omega). \quad (16)$$

The spectra $E^{L,NL}(k_0, \omega)$, $E^{L,NL}(\omega)$ and $E^{L,NL}(k_0)$ are normalized by the total energy $E_{\text{tot}}^{L,NL}$ to facilitate comparison between different parametric cases. In Eq. (13) the averaging extends over the interval $k_0 - 0.5 \leq |\mathbf{k} = (k_x, k_y, k_z)| < k_0 + 0.5$ due to the Cartesian grid discretization $k_x, k_y, k_z = -N/2, \dots, -1, 0, 1, \dots, N/2$ where N is the resolution of the DNS, such that \mathbf{k} is rarely equal to k_0 .

Figure 9 shows the distribution in (k, ω) space of the kinetic energy density spectra $E^{L,NL}(k_0, \omega)$ for the linear and nonlinear simulations. The dashed line in the plots also indicate the maximum frequency $2\Omega_z$ available for IWs from the dispersion relation. As expected, the spectral kinetic energy density is concentrated on the forcing frequency ω_f in the linear [Fig. 9(a)] and nonlinear simulations [Fig. 9(b)]. However, whatever the spatial scale k , there is more energy in the frequency domain around the peak at ω_f in the nonlinear case than in the linear case. This spread is therefore linked to the redistribution of energy via nonlinear mechanisms. The concentration of energy along constant k lines shows that some scales are more energetic than others. In the linear and nonlinear simulations, we observe a global decrease of energy as the timescale related to the spectral modes decreases, i.e., when k increases. This phenomenon is more marked in the linear case beyond $k = 50$. Moreover, some harmonics of the form $n\omega_f$, $n = 2, 3, \dots, 7$ appear as a concentration of energy along constant ω lines, which persist whatever the scale k . The origin of these harmonic frequencies is linked to the constant part of the forcing term that reflects the vertical displacement of the torus in Eq. (5). This term is $-\frac{1}{\eta} \mathbf{u}_s \hat{H}^T(\mathbf{x}, t)$ in physical space, and $-\frac{1}{\eta} \dot{z}(t) \hat{H}_0^T(k, \theta(\mathbf{k})) e^{-ik_z z(t)}$ in spatial

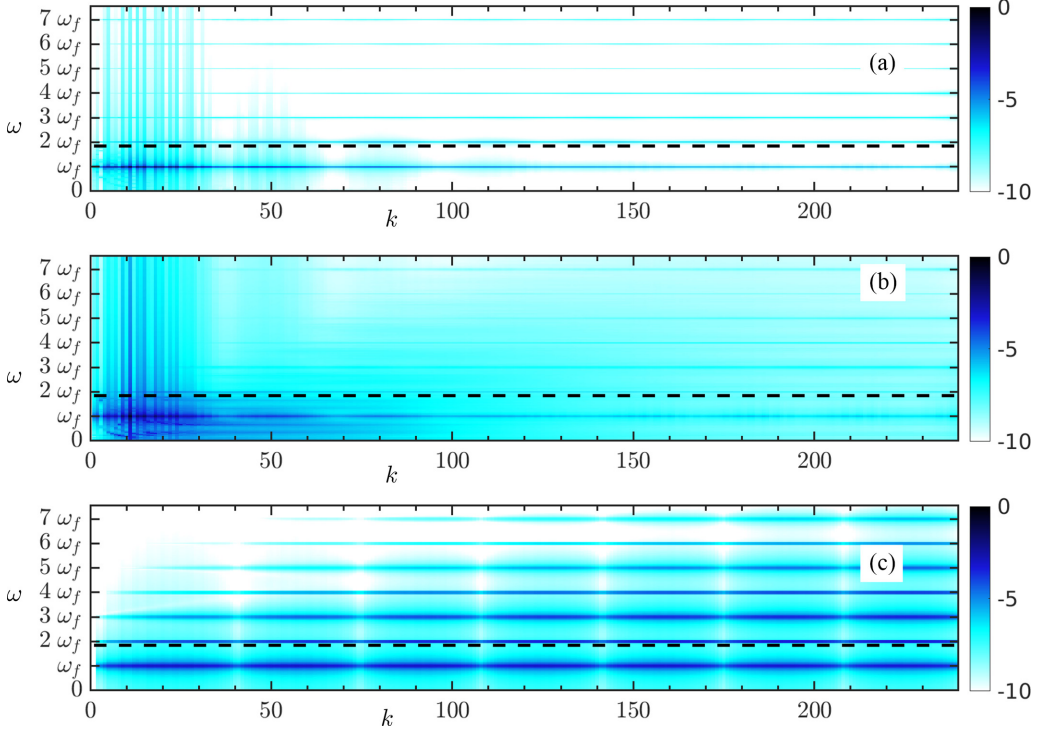


FIG. 9. Normalized spatiotemporal spectra: (a) linear simulation spectrum $E^L(k, \omega)/E_{\text{tot}}^L$; (b) nonlinear simulation spectrum $E^{\text{NL}}(k, \omega)/E_{\text{tot}}^{\text{NL}}$; (c) forced case spectrum $E^f(k_0, \omega)/E_{\text{tot}}^f$. The dashed line represents the rotating rate $2\Omega_z$. The color bars indicate the log of the amplitude of the spectra.

Fourier space as discussed in Appendix A. When applying the temporal Fourier transform noted \mathcal{F}_t , the spatiotemporal spectrum of forcing is

$$E^f(k_0, \omega) = \sum_{k_0-0.5 \leq |k| < k_0+0.5} |\hat{H}_0^T(k, \theta(\mathbf{k})) \mathcal{F}_t[\dot{z}(t)e^{-ik_z z(t)}](\omega)|^2. \quad (17)$$

As in Eqs. (14), (15), and (16) for the spectra of kinetic energy density, one defines in (17) similar spectra for the forcing: total temporal spectrum $E^f(\omega) = \sum_k E^f(k, \omega)$, total spatial spectrum $E^f(k) = \sum_\omega E^f(k, \omega)$, and total forcing $E_{\text{tot}}^f = \sum_{k, \omega} E^f(k, \omega)$. Figure 9(c) for the normalized energy $E^f(k_0, \omega)/E_{\text{tot}}^f$ shows that the forcing induces harmonic frequencies $n\omega_f$ which are also visible in the linear and nonlinear spectra, and, surprisingly, their energies do not decrease with scale. Harmonic forcing seems also to be found in experiments that generate the harmonics of waves, as in the case of a cylinder oscillating in a rotating fluid with a residual nonharmonic component of the oscillation profile of the wave generator [36]. The harmonics of IWs do not appear in our simulations wherein the condition $n\omega \leq 2\Omega_z$ for their appearance is not met.

In order to analyze the spectra more precisely, we plot the spectra as functions of ω for the linear and nonlinear simulations in Fig. 10. Figures 10(a) and 10(b) show the normalized energy density spectra $E^{\text{L,NL}}(k_0, \omega)$ at $k_0 = 25$ and $k_0 = 50$, respectively. Figure 10(c) shows the total temporal spectrum $E^{\text{L,NL}}(\omega)$. The corresponding forcing spectrum E^f is also shown in the three figures.

The power law ω^{-2} found by Le Reun *et al.* [60] in wave turbulence for rotating fluid is shown in Figs. 10(a) and 10(b). For nonlinear simulations, the spectrum at large spatial scale $E^{\text{NL}}(k = 25, \omega)$ in 10(a) is consistent with the ω^{-2} scaling at frequencies smaller than the forcing one ω_f with a large peak similar to that found in weak inertial-wave turbulence experiments (see Monsalve *et al.* [61]).

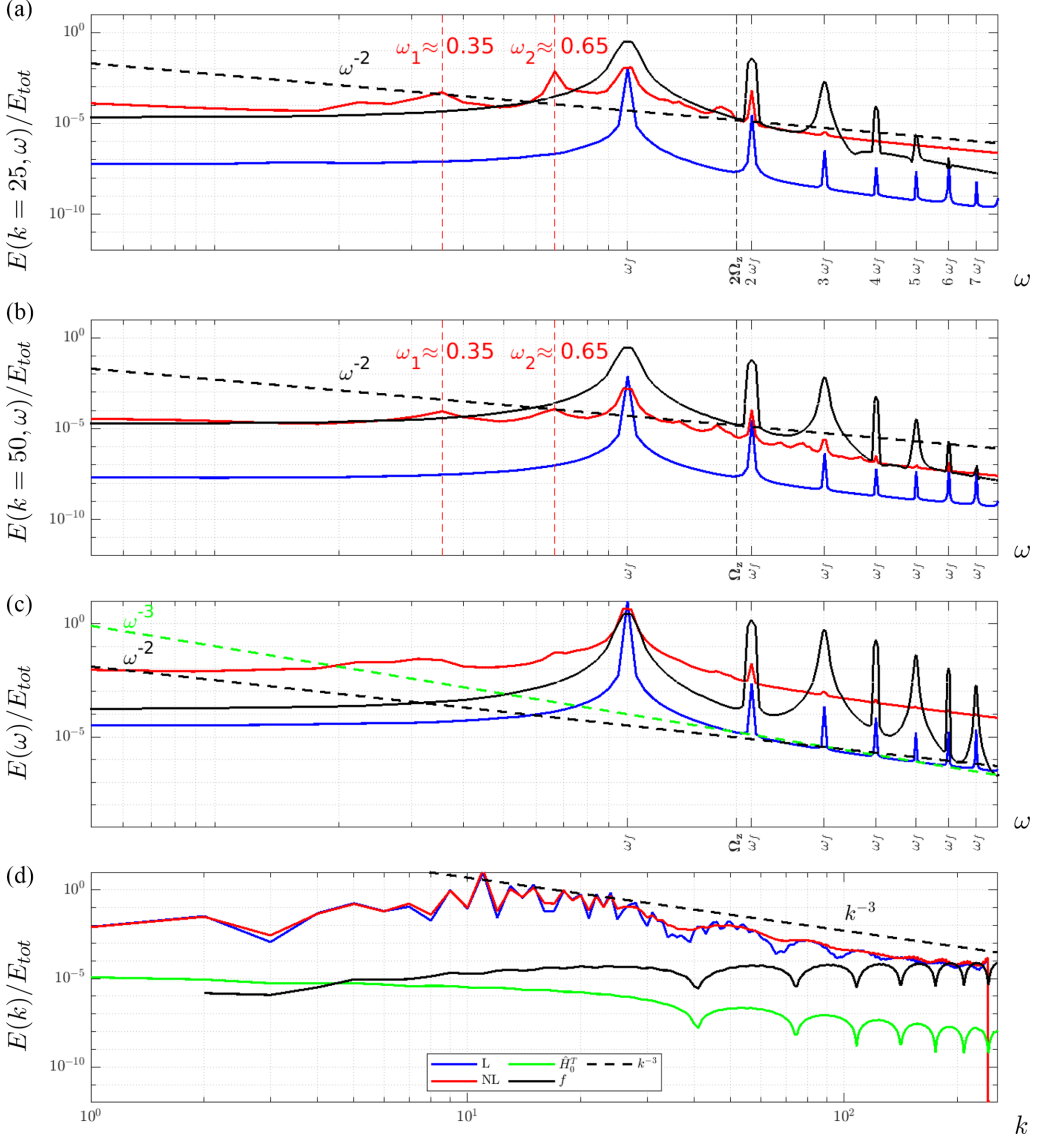


FIG. 10. Normalized spatiotemporal spectra $E^{L, NL}(k, \omega)/E_{tot}^{L, NL}$ and $E^f(k, \omega)/E_{tot}^f$ for (a) slice at $k = 25$; (b) slice at $k = 50$. (c) Normalized total temporal spectrum $E^{L, NL}(\omega)/E_{tot}^{L, NL}$, $E^f(\omega)/E_{tot}^f$. (d) Normalized spatial spectrum $E^{L, NL}(k)/E_{tot}^{L, NL}$, $E^f(k)/E_{tot}^f$, and $\hat{H}_0^T(k)$ from (19). The blue, red, and black curves are, respectively, for the linear, nonlinear, and constant forcing term. The green curve for $\hat{H}_0^T(k)$ has been shifted by $\times 10^{-4}$, and the black curve for $E^f(k)/E_{tot}^f$ has been shifted by $\times 10^{-2}$ for better comparison. The dashed black lines represent the power laws ω^{-2} and k^{-3} suggested by Le Reun *et al.* [60].

The spectrum $E^{NL}(k = 50, \omega)$ [Fig. 10(b)] at smaller spatial scale is steeper. The wave turbulence frequency scaling is not retrieved at all spatial scales.

As expected, all the spectra in Figs. 10(a), 10(b), and 10(c) have a frequency peak at forcing frequency ω_f . As shown above in Eq. (17), the constant part of the forcing contains the displacement term $\mathcal{F}_1[\dot{z}(t)e^{-ik_z z(t)}](\omega)$ which triggers the harmonics $n\omega_f$. Moreover the associated amplitude of forcing decreases with ω but not between scales when comparing the spectra at $k = 25$ and $k = 50$.

This constant part of forcing is therefore responsible for the peaks observed at harmonic frequencies for linear and nonlinear simulations in Figs. 10(a) and 10(b).

However, in nonlinear simulations, the peaks of energy spectrum are smoothed out by nonlinearities, with enlarged bandwidths around the harmonics $n\omega_f$. This is associated to local redistribution and a slightly off-resonant transfer of energy across scales. Moreover, for frequencies smaller than ω_f , we observe a difference between linear and nonlinear regimes. In the latter, two secondary peaks are visible at smaller frequencies $\omega_1 \simeq 0.35\omega_f$ and $\omega_2 \simeq 0.65\omega_f$ in the spectra at $k_0 = 25$ and $k_0 = 50$ such that

$$\omega_1 + \omega_2 \simeq \omega_f. \quad (18)$$

This is a typical signature of wave turbulence based on the triadic resonant condition for IWs, namely, $\omega_{dr}(\mathbf{k}) = \omega_{dr}(\mathbf{p}) + \omega_{dr}(\mathbf{q})$ and $\mathbf{k} = \mathbf{p} + \mathbf{q}$ [47,62], and was also recently observed by Shmakova *et al.* [20] for torus configuration in a stratified fluid. The total time spectrum $E^{\text{NL}}(\omega)$ in Fig. 10(c) also contains the same two peaks although less marked than for the spectra at fixed $k = 25$ and $k = 50$. Although triadic exchanges are a feature of spectral nonlinear terms in turbulence—expressed as a convolution integral over spectral modes satisfying $\mathbf{k} = \mathbf{p} + \mathbf{q}$ —they do not necessarily correspond to inertial wave resonance interactions, all the more so since the energy injection does not control which individual modes are forced. Nevertheless, in Sec. VB we shall show that the spectrum is indeed dominated by IWs in our simulations, so that the observed peaks at ω_1 and ω_2 are actual IWs.

The total spatial spectrum of the kinetic energy density $E(k)$ is shown in Fig. 10(d). For linear and nonlinear simulations, it also contains periodic bumps at certain scales that are directly linked to the spectrum $E^f(k)$ of the forcing term (black solid curve) and hence to the spectral trace of the mask function $\hat{H}_0^T(k, \theta(\mathbf{k}))$ [Eq. (A2)] that represents the torus geometry. Averaging over all orientations of \mathbf{k} at a given scale k_0 on a Cartesian grid, one gets

$$\hat{H}_0^T(k_0) = \sum_{|\mathbf{k}|=k_0} \hat{H}_0^T(k, \theta(\mathbf{k})), \quad (19)$$

which is plotted in Fig. 10(d) (green solid curve), and is at the origin of the bumps. The bumps are visible at small scale for linear and nonlinear simulations, but they are smoother in the nonlinear regime due to local turbulent diffusion. Figure 10(d) also shows the power law k^{-3} suggested in several studies [60,63,64], which is consistent with our numerical results.

B. Signature of IWs

The above spectral analysis demonstrates the necessity to assess and quantify precisely the presence of IWs in the torus configuration. A mere space-time spectrum function in (k, ω) is not sufficient, because an angular space-time spectrum function in (k, ω, θ) is required to assign angles θ to wavevectors and their dispersion relation [geometry in Fig. 1(a)]. As in Lam *et al.* [57], we define angular spectra

$$E^{\text{L,NL}}(\theta_0, k_0, \omega) = \sum_{\substack{k_0 - 0.5 \leq |\mathbf{k}| < k_0 + 0.5 \\ \theta_0 - \Delta\theta \leq \theta(\mathbf{k}) < \theta_0 + \Delta\theta}} |\tilde{\mathbf{u}}^{\text{L,NL}}(\mathbf{k}, \omega)|^2. \quad (20)$$

We select spectral angles in the interval $\theta_0 - \Delta\theta \leq \theta(\mathbf{k}) < \theta_0 + \Delta\theta$ with $\Delta\theta = 0.5^\circ$.

The normalized spectra $E^{\text{L,NL}}(\theta, k, \omega)/E_{\text{tot}}^{\text{L,NL}}$ at scales $k = 25$ and $k = 50$ used in Sec. VA are shown in Fig. 11. The color range is adapted to the maximum of each spectrum. Note that the stripey aspect of the plots is due to the forcing geometry, as explained in Appendix C.

In the linear case [see Figs. 11(a) and 11(c)], the energy is concentrated in the harmonics of the forcing, and the dispersion relation is observable for $k = 25$ and less so for $k = 50$, showing that waves are present at smaller scales where the dissipation, although small, is significant with respect to the forcing. Note the presence of four peaks of energy density due to the resonance phenomenon

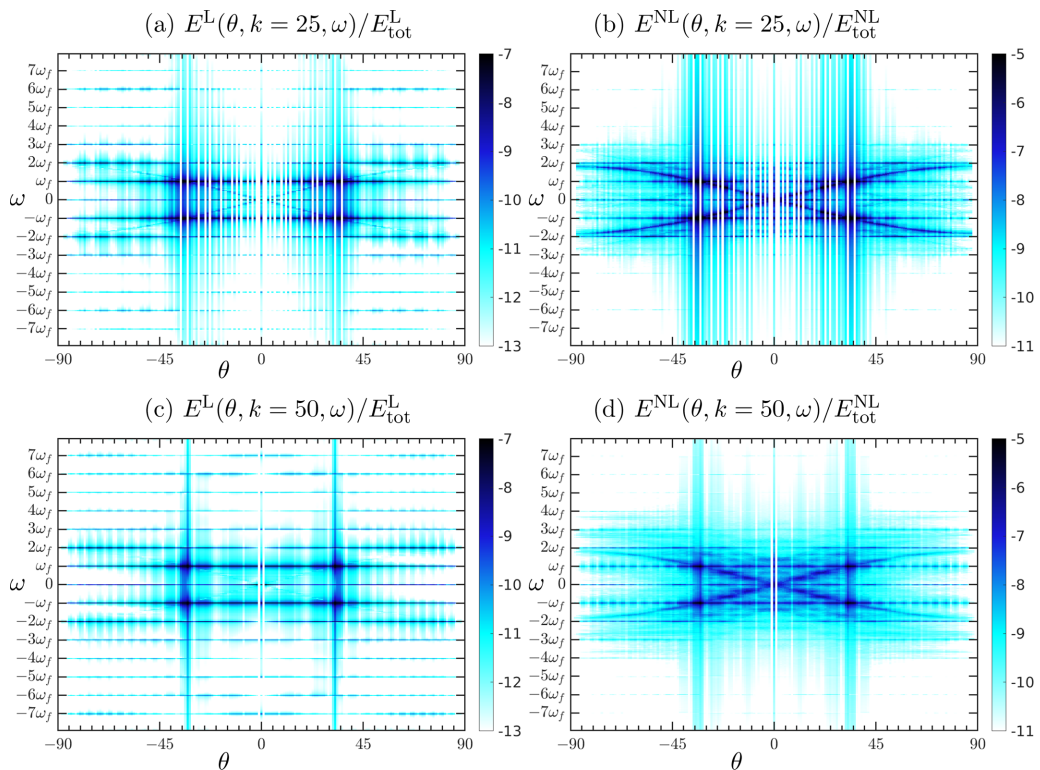


FIG. 11. Spectral kinetic energy density $E^{L,NL}(\theta, k, \omega)/E_{\text{tot}}^{L,NL}$ for scales $k = 25$ and $k = 50$ for $\theta_f = 33^\circ$. Panels (a) and (b) are for $k = 25$, (c) and (d) are for $k = 50$; (a) and (c) are for linear simulations, (b) and (d) are for nonlinear simulations. Color bar in log of amplitude.

when the frequency of the forcing ω_f is equal to the natural frequency of the IW associated with the propagation angle θ_f , i.e., when $\omega_f = \omega_{dr}(\theta_f)$. In the nonlinear simulations in Figs. 11(b) and 11(d), the energy is less concentrated on the harmonics of forcing and more on the dispersion relation than in the linear simulations. We also observe a diffusion of the energy around the curve of the dispersion relation, as in stratified and rotating turbulence [65]. In both cases, at $k = 25$ and $k = 50$, the waves are dominant compared to the linear case. Combined with the results of Sec. V A, one concludes that the triadic resonance of IWs appears in the flow and maintains the presence of waves at different scales.

The total angular spectrum of all scales, is obtained by accumulating the angular spectrum of each scale (20) as

$$E^{L,NL}(\theta, \omega) = \sum_k E^{L,NL}(\theta, k, \omega). \quad (21)$$

$E^{L,NL}(\theta, \omega)$ is shown in Figs. 12(a) and 12(b), with the same color range for the linear and nonlinear simulations. In both cases, the energy distribution is concentrated along the dispersion relation of the IWs $\omega = \omega_{dr}(\theta)$ given by (1) as a signature of IWs, so that, overall, the kinetic energy seems to be contained mostly in IWs. However, in the nonlinear simulation, the above-described harmonic frequencies due to forcing are limited to $2\omega_f$ and to a lesser extent to $3\omega_f$, whereas in the linear case the higher harmonic frequencies $3\omega_f, 4\omega_f, \dots, 7\omega_f$ are strongly persistent for any θ . Moreover, the energy concentration around the dispersion relation is sharper in the linear case than in the nonlinear simulation where it is locally diffused. Again, this suggests that a nonlinear mechanism

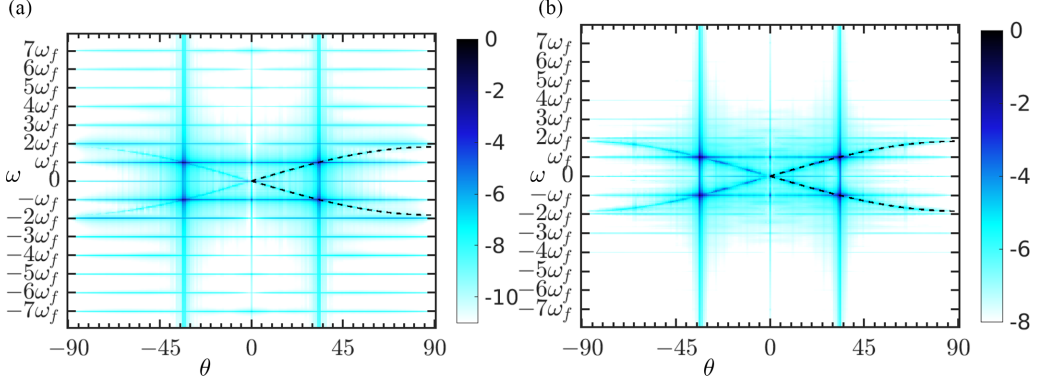


FIG. 12. Total angular spectral kinetic energy density $E^{L,NL}(\theta, k_0, \omega)/E_{\text{tot}}^{L,NL}$ for $\theta_f = 33^\circ$: (a) for linear simulation spectrum (label L); (b) for nonlinear simulation spectrum (label NL). The color bar indicates the log of amplitude. The dashed line represents the dispersion relation $\omega_{dr}(\theta)$ given by (1).

such as triadic resonance of IWs enhances the presence of waves compared to linear phenomena. To explain this mechanism, quantitative theory would have to take into account triadic interactions, which are one of the key elements in our analysis of the flow.

C. Nonlinear interaction in the focal zone

As shown in Sec. IV, the focal zone is the most intense zone in terms of dissipation, and the bulk flow is practically dominated by IWs. We now need to link these two observations by studying the nonlinear interaction that takes place in the focal zone. For this, we rely on a bispectrum analysis of the vertical velocity field u_z .

We start by showing in Figs. 13(a) and 13(b) the time oscillations of $u_z(\mathbf{x}_0, t)$ for linear and nonlinear simulations, respectively, at a point $\mathbf{x}_0 = (0, 0, Z_f)$ in the focal zone. Velocity oscillations are regular in the linear case [Fig. 13(a)] but modulated in amplitude in the nonlinear one [Fig. 13(b)]. As expected, a wide peak of energy at frequency ω_f and secondary peaks at harmonic frequencies $n\omega_f$ appear in Fig. 13(c) for the total time spectrum $E_z(\omega)$ of $u_z(\mathbf{x}_0, t)$ and for linear and nonlinear simulations. The spectrum of the nonlinear simulation [Fig. 13(c)] differs from that of the linear simulation by a much larger level of background vertical kinetic energy at all frequencies than in the linear simulation, attesting of nonlinear enrichment of the spectrum. The two time spectra obtained at the focal point \mathbf{x}_0 are consistent with the spectra obtained in the complete domain in the nonlinear and linear simulations in Fig. 10(c), although in the latter plot the peaks are sharper.

We characterize the spectral enrichment by nonlinear interactions in the focal zone using a bispectral analysis. For this, we consider the Fourier transform of the third-order cumulant function, which is the bispectrum that measures the statistical dependence between three spectral components $(\omega_1, \omega_2, \omega_3)$ satisfying the resonance condition of the frequencies $\omega_3 = \omega_2 + \omega_1$, a condition deriving from the nonlinear terms in the energy balance equations [64]. We compute these statistics by using the HOSA Matlab toolbox proposed by Swami *et al.* [66]. The vertical velocity signal $u_z(t)$ is decomposed into $N = 379$ segments with 99% overlap between them, and we apply Hamming windowing on each segment containing the velocity $u_z^i(\mathbf{x}_0, t)$, $i = 1, \dots, N$. The FFTs are computed with 2048 points. The bispectrum of the i th segment is calculated as

$$b^i(\omega_1, \omega_2) = \hat{u}_z^i(\omega_1)\hat{u}_z^i(\omega_2)\overline{\hat{u}_z^i(\omega_1 + \omega_2)}, \quad (22)$$

where \hat{u}_z^i represents the FFT on the i th segment of $u_z^i(\mathbf{x}_0, t)$ and $\bar{*}$ is the complex conjugate. The power spectrum of $b^i(\omega_1, \omega_2)$ is $|b^i(\omega_1, \omega_2)|^2$. The bispectrum is estimated by averaging all

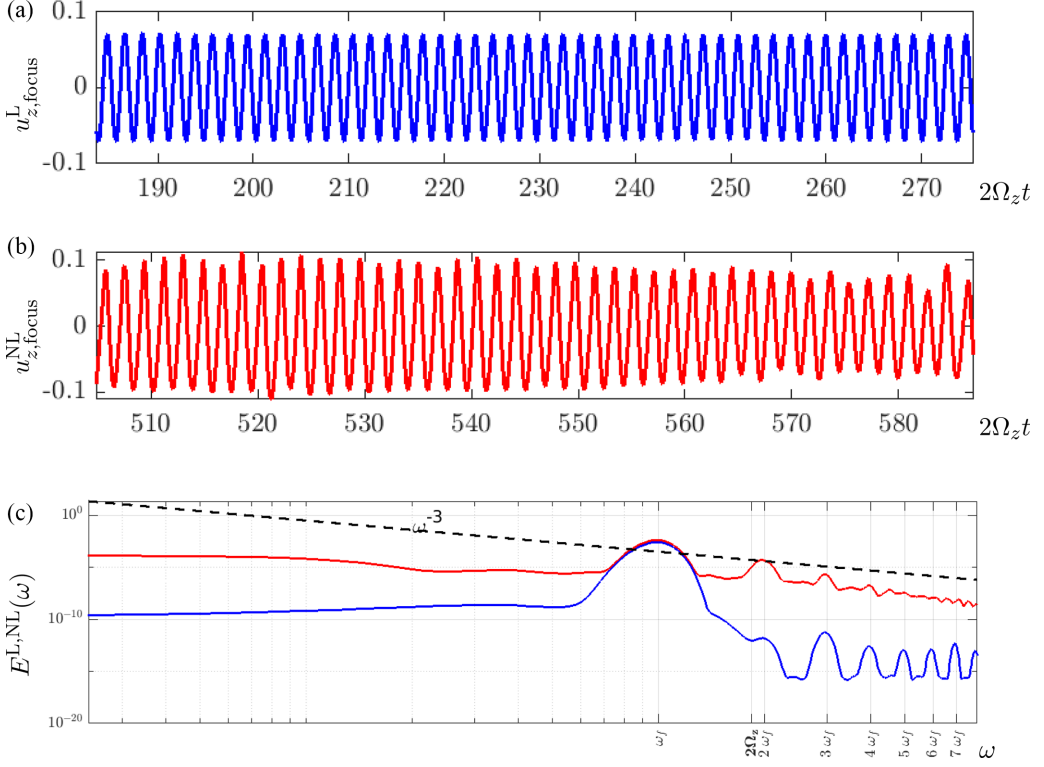


FIG. 13. Vertical velocity signal $u_z(\mathbf{x}_0, t)$ as a function of normalized time $2\omega_z t$ in the focal zone by the simulation of the torus configuration at $\theta_f = 33^\circ$: (a) linear simulation; (b) nonlinear simulation; (c) temporal spectrum energy $E(\omega)$ in blue for linear simulations, and red for the nonlinear ones.

segments noted (*), as

$$\langle |b(\omega_1, \omega_2)|^2 \rangle = \sum_{i=1}^N |b^i(\omega_1, \omega_2)|^2. \quad (23)$$

The bicoherence is the normalized bispectrum

$$B(\omega_1, \omega_2) = \frac{\langle |b(\omega_1, \omega_2)|^2 \rangle}{\langle |\hat{u}_z(\omega_1)|^2 \rangle \langle |\hat{u}_z(\omega_2)|^2 \rangle \langle |\hat{u}_z(\omega_1 + \omega_2)|^2 \rangle}. \quad (24)$$

Note that $\langle |\hat{u}_z(\omega_1)|^2 \rangle$, $\langle |\hat{u}_z(\omega_2)|^2 \rangle$, and $\langle |\hat{u}_z(\omega_1 + \omega_2)|^2 \rangle$ are the classical power spectra for the frequencies ω_1 , ω_2 and $\omega_1 + \omega_2$.

Figure 14(a) is the map of bicoherence $B(\omega_1, \omega_2)$ for the linear simulation and Fig. 14(b) for the nonlinear simulation (note the different scales). For the same resolution and same numerical parameters, the nonlinear data are overall more concentrated around the peak than that in the linear case, which reveals the importance of nonlinear interactions. For any fixed frequency ω_3 with a spectrum $E(\omega_3)$ as in Fig. 13(c), the bicoherence function $B(\omega_1, \omega_2)$ measures the statistical dependence of ω_3 on a combination of frequency pairs (ω_1, ω_2) such that $\omega_3 = \omega_1 + \omega_2$. The chosen frequency ω_3 appears on the maps of $B(\omega_1, \omega_2)$ in Figs. 14(a) and 14(b) as an oblique line passing from top left to bottom right, defined by the affine equation $\omega_2 = \omega_3 - \omega_1$. For example, the highest frequencies resulting from the dispersion relation are $\omega_3 = \pm 2\Omega$ and are represented as diagonal dashed black lines in Figs. 14(a) and 14(b). The highest frequencies of the waves are $\omega_1 = \pm 2\Omega$ and $\omega_2 = \pm 2\Omega$ (vertical and horizontal dashed black lines, respectively), meaning that an interaction

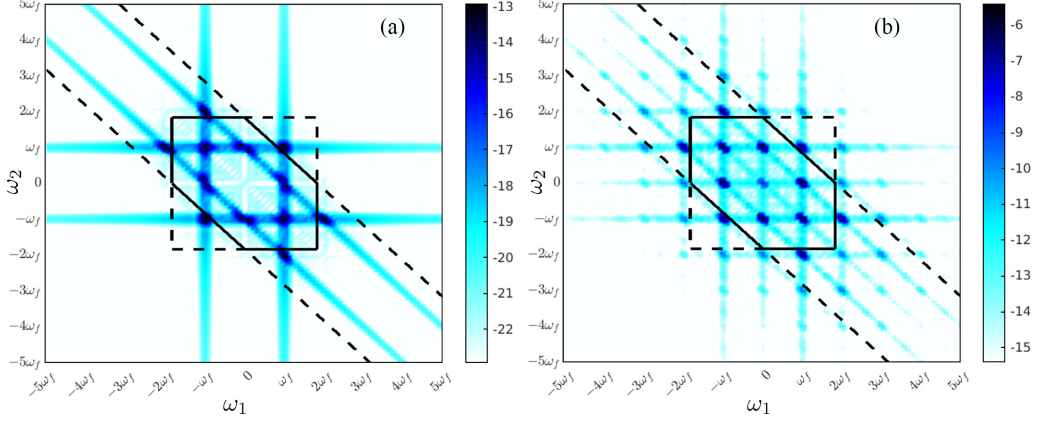


FIG. 14. Bicoherence contours obtained at $\theta_f = 33^\circ$: (a) linear simulation; (b) nonlinear simulation. Color bar indicates the log of amplitude. The hexagon (solid black line) represents the domain of nonlinear interaction of IWs. The dotted line represent highest frequencies ($\pm 2\Omega$) of the IWs.

between the waves produces a frequency ω_3 in the square $\omega_1 = \pm 2\Omega$ and $\omega_2 = \pm 2\Omega$. If this frequency ω_3 is a frequency of waves, then this square is limited by the two oblique lines $\omega_3 = \pm 2\Omega$: the irregular hexagon drawn as a solid black line therefore represents the nonlinear interaction of IWs. Within this hexagon, the frequencies ω_1 and ω_2 and their interaction $\omega_3 = \omega_1 + \omega_2$ satisfy the dispersion relation of IWs (1), namely, $\omega_3 = \omega_{dr}(\mathbf{k})$, $\omega_2 = \omega_{dr}(\mathbf{p})$ and $\omega_1 = \omega_{dr}(\mathbf{q})$ with \mathbf{k} , \mathbf{p} , and \mathbf{q} the wave vectors of waves satisfying the triadic resonant condition $\omega_{dr}(\mathbf{k}) = \omega_{dr}(\mathbf{p}) + \omega_{dr}(\mathbf{q})$.

In the linear simulations, the convective nonlinear term $\boldsymbol{\omega} \times \mathbf{u} = \mathbf{0}$, but there is still a nonlinear interaction due to the penalization term (5), in particular for the torus forcing term $-\frac{1}{\eta} \mathbf{u}_s H^T(\mathbf{x}, t)$ that produces harmonics from temporal nonlinear interactions due to multiplication in Fourier space, as seen in Sec. V A [the term $\mathcal{F}_t[\tilde{z}(t)e^{-ik_z z(t)}](\omega)$ in Eq. (17)]. According to $B(\omega_1, \omega_2)$ [Fig. 14(a)], most of the interactions take place in the hexagon of the IWs, and three oblique lines corresponding to the frequencies $\omega_3 = 0, \omega_f, 2\omega_f$ are visible. From $B(\omega_1, \omega_2)$, it can be deduced that

(1) Stationary modes $\omega_3 = 0$ are the geostrophic modes (see Sec. III B), which are due to one interaction between the waves ($\omega_1 = \omega_f, \omega_2 = -\omega_f$) and its symmetric part ($\omega_1 = -\omega_f, \omega_2 = \omega_f$) and

(2) The frequency $\omega_3 = 2\omega_f$ (highest frequency out of the dispersion relation) is due to one interaction between waves ($\omega_1 = \omega_f, \omega_2 = \omega_f$).

Note that the main frequency of the waves is imposed by the forcing at ω_f (see Sec. V B). For the frequency $\omega_3 = \omega_f$, there are two different interactions between the stationary modes (geostrophic modes) and the waves ($\omega_1 = 0, \omega_2 = \omega_f$) and between the waves ($\omega_1 = -\omega_f, \omega_2 = 2\omega_f$) and their symmetric part.

In the nonlinear simulations [Fig. 14(b)], unlike linear ones, we observe many more interactions indicated by peaks of the bicoherence function, in particular in the hexagon. This means that triadic resonance-type interactions seem to dominate all other interactions. Moreover, the stationary mode at $\omega_3 = 0$, identified as central and secondary vortices in Sec. III B, is due to other interactions such as those between waves ($\omega_1 = 2\omega_f, \omega_2 = -2\omega_f$) and waves ($\omega_1 = 3\omega_f, \omega_2 = -3\omega_f$). In addition, there are interactions between the higher harmonics $\pm 2\omega_f, \pm 3\omega_f, \dots$ and the waves at $\pm\omega_f$, or in general with the higher harmonics $\pm 2\omega_f, \pm 3\omega_f, \dots$. This frequency enhancement between linear and nonlinear simulations is linked to the introduction of the nonlinear convective term and reflects a transfer between the waves and between the harmonics and the waves. This is not observed in the linear simulations [Fig. 14(a)].

VI. CONCLUSION

Using direct numerical simulations, we study the focusing of IWs caused by the oscillation of a torus in a fluid with background rotation. Two models for representing the oscillating torus are considered: a Dirac ring configuration, which allows us to compare the results with those from the linear theory developed by Liu *et al.* [23], and a 3D solid torus representing closely the experimental realizations, and allowing us to extrapolate the analytical results to a more complex configuration. For a Dirac ring configuration, only linear simulations are considered, whereas for the 3D torus, linear and nonlinear simulations are performed to better understand the limits of the linear approach. For all the simulations, the frequency ω_f of the torus oscillations was fixed but the rotation rate of the fluid background Ω_z was varied to vary the angle of the waves emitted by the torus or by the ring of Dirac. In so doing, only the Rossby number $\text{Ro} \ll 1$ varies with the propagation angle for forcings by the Dirac ring or by the 3D torus, and the other nondimensional numbers—Reynolds Re , Keulegan-Carpenter Ke , and Stokes St —are fixed. For the 3D torus configuration, since the Stokes number is large $\text{St} \gg 1$, the waves have a bimodal structure in agreement with the linear theory of Shmakova *et al.* [20] with a maximum of vertical velocity in focal zone.

Our first result concerns the averaged main flow for the 3D torus configuration. In the linear case, the average main flow appears in the form of a flow invariant along z (axis of rotation) and could be assimilated to a geostrophic mode. The flow consists of two contra-rotating cylinders. In the nonlinear case, the averaged main flow is mainly dominated by a central vortex whose formation seems to be in agreement with the linear theory of Ranjan and Davidson [44]. We thus observe the generation of a mean flow with central vortex only due to the nonlinear focusing of the waves in agreement with the mechanisms related to a patch of turbulence described by these authors.

In addition, we have shown that the maximum of the vertical velocity in the focal zone is consistent with the linear theory for the Dirac ring configuration [23]. Indeed, the curves for the numerically measured and theoretically predicted vertical velocities overlap and reach a maximum at propagation angle $\theta_f = 35^\circ$. This ring of Dirac configuration serves as a guide and benchmark before considering the case of the 3D torus for which the maximum amplification is at around $\theta_f = 30^\circ$. Moreover, for this angle, the dissipation in the focal zone appears to reach a maximum, which is always more important in the nonlinear than in the linear case.

Finally, using a four-dimensional spatiotemporal analysis, we have shown that the flow is dominated by IWs on a wide range of scales that we precisely identify. The observed wave scales can be smaller in the nonlinear case than in the linear case, suggesting the existence of a nonlinear transfer that reinforces the presence of IWs despite the presence of harmonics. This mechanism seems to be linked to triadic resonant interactions. The harmonic frequencies are induced by the torus oscillation on all scales. We have performed a bicoherence analysis in the focal area to identify nonlinear interactions. In the nonlinear case, it turns out that the triadic resonant interactions of the waves dominate all other interactions.

A possible extension of the present study to get even closer to the oceanographic context would involve the inclusion of the effect of local variations in topography on the production of waves of different phases and their focusing, by considering a torus with azimuthal variations of shape or radius. Our study also calls for the development of a weakly nonlinear theory to reach beyond existing linear theories, to take into account nonlinear interactions between waves and better predict mixing in the ocean that takes place in the presence of stratification. One question concerns the stability of the central vortex. In another way, the subcritical or supercritical nature of the instability could be explored in order to determine the effects of hysteresis around the threshold of the instability. We have simulated a wave regime; however, it will also be necessary to explore regimes with higher Reynolds numbers that are beyond the scope of this study. Our work falls within the scope of studies aimed at quantifying the intense events linked to wave focusing in order to make a significant contribution to the global energy balance.

ACKNOWLEDGMENTS

This research was funded by Agence Nationale de la Recherche (FundRef registry number 10.13039/501100001665) under Grant No. ANR-18-CE92-0034-01. This work was granted access to the HPC resources of IDRIS under the allocation A0102A02206 made by GENCI and HPC ressources of the PMCS2I computing center of Ecole centrale de Lyon, partner of EQUIPEX EQUIP@MESO. We would like to thank Prof. P. A. Davidson for fruitful discussions.

The authors report no conflict of interest.

APPENDIX A: COMPARED INJECTED POWER BY DIRAC RING AND 3D TORUS FORCINGS

The two configurations do not inject the same energy distribution into the focal point or the focal zone. In the first approximation, the energy sent by the forcing \mathbf{f} depends directly on the spatial functions H_0^T or H_0^{DR} . This comes from the physical space power equation at t and \mathbf{x} obtained by multiplying (2) by $\mathbf{u}(\mathbf{x}, t)$. Equivalently, the spectral power equation at t and \mathbf{k} is obtained by Fourier transforming (2) and multiplying it by the velocity Fourier component $\hat{\mathbf{u}}(\mathbf{k}, t)$, and adding the complex conjugate. This yields Lin's equation for spectral energy density in isotropic homogeneous turbulence [67] when averaging on the set of wave vectors with the same modulus. The advantage of Fourier space is to interpret the power equation in terms of scale. Integrating these power equations over the entire physical or Fourier domain provides two ways of obtaining the same kinetic energy evolution equations. In Fourier space, the injected power forcing is given by the inner product $\hat{\mathbf{f}}(\mathbf{k}, t) \cdot \overline{\hat{\mathbf{u}}(\mathbf{k}, t)} + CC$ where $\bar{*}$ is the complex conjugate of $*$, $\hat{*}$ is the spatial Fourier transform, and CC means that we add the complex conjugate of the previous expression. Since $\hat{H}_0^T(\mathbf{k})$ and $\hat{H}_0^{DR}(\mathbf{k})$ are the Fourier transforms of H_0^T and H_0^{DR} , the injected power includes terms as $A_0 \sin(\omega_f t) \hat{H}_0^T(\mathbf{k}) \cdot \overline{\hat{\mathbf{u}}(\mathbf{k}, t)}$ in the Dirac ring case and $-\frac{1}{\eta} \dot{z}(t) \hat{H}_0^T(\mathbf{k}) e^{-ik_z z(t)} \cdot \overline{\hat{\mathbf{u}}(\mathbf{k}, t)}$ in the 3D torus case. \hat{H}_0^T and \hat{H}_0^T therefore act as transfer functions in Fourier space that spatially filter the velocity field.

Due to axisymmetry, we express H_0^T and H_0^{DR} in polar coordinates (k, θ) , where $k = |\mathbf{k}|$, $\theta = \tan^{-1}(k_z/k_h)$ and $k_h = (k_x^2 + k_y^2)^{1/2}$. The expressions for \hat{H}_0^T and \hat{H}_0^{DR} are given in Liu *et al.* [23] and Beleggia *et al.* [68] as

$$\hat{H}_0^{DR}(k_h, \theta) = 2\pi J_0(k_h \cos \theta), \quad (\text{A1})$$

$$\hat{H}_0^T(k, \theta) = \frac{4\pi}{k \sin \theta} \int_{-b}^b J_0[k \cos \theta (a + x)] \sin(k \sin \theta \sqrt{b^2 - x^2}) (a + x) dx, \quad (\text{A2})$$

where J_0 is the zeroth-order Bessel function of the first kind. In Eq. (A1), the geometrical parameter is the radius $a = 1$ for the case of Dirac ring, and in Eq. (A2) $a = 0.848$ and $b = 0.0942$ for the 3D torus. The amplitude maps in (θ, k) of $|\hat{H}_0^T(k, \theta)|$ and $|\hat{H}_0^{DR}(k, \theta)|$ from these equations are plotted in Fig. 15 using explicit numerical integration for all θ except for $\theta = 0$ where the calculation diverges. The distribution of the mask functions show the dependence in Fourier space of the energy input in the system since they enter the definition of the forcing \mathbf{f} . Figure 15 therefore shows that $|\hat{H}_0^T(k, \theta)|$ and $|\hat{H}_0^{DR}(k, \theta)|$ let the energy pass to all angles θ for both configurations, but also that, for the 3D torus configuration, energy is concentrated at large scales from small k up to $k \simeq 30$, while for the Dirac ring, it extends to all resolved scales. Moreover, the figure shows that, although energy at the forcing frequency ω_f is sent to all angles and scales, only a small part goes into the wave vector \mathbf{k} that corresponds to the precise angle θ_f from the dispersion relation (8).

APPENDIX B: SOURCE DISCRETIZATION EFFECT ON THE ENERGY TRANSFER

As noted by Boury *et al.* [55] in their experimental work, in a confined domain, whether in numerical simulations or in experiments, each wave vector allowed in such a confined geometry is

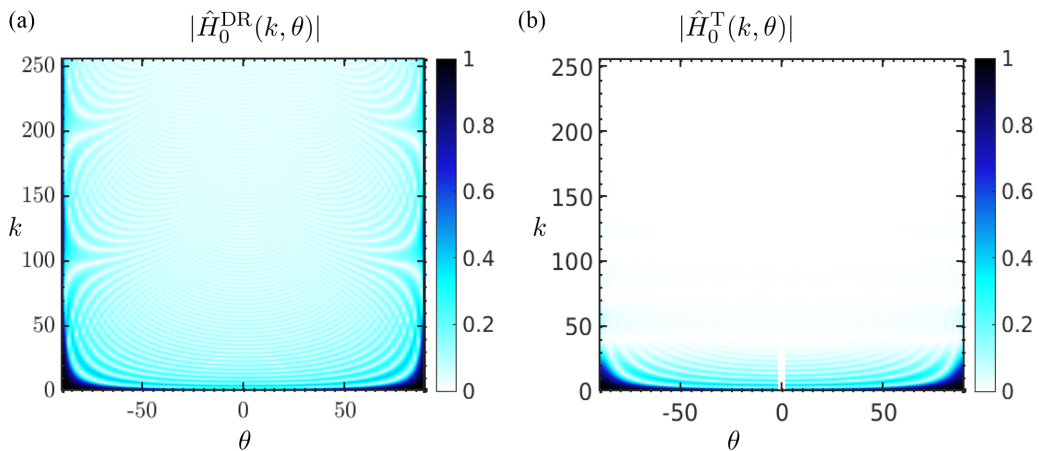


FIG. 15. Absolute value of forcing terms in Fourier space ($k \equiv |\mathbf{k}|$, θ): (a) ring of Dirac $|\hat{H}_0^{\text{DR}}(k, \theta)|$; (b) 3D torus $|\hat{H}_0^{\text{T}}(k, \theta)|$. Both functions are normalized by their maximum value.

quantified with a discrete collection of wave numbers in each direction. In a 2π -periodic domain, the wave vectors \mathbf{k} are a set of integers $\mathbf{k} = (l, m, n)$. If small scales can be described by a multitude of wave numbers, this is no longer the case for large scales, where only a few wave numbers represents them. For instance, for a wave number $k = 1$, there are only six possible wave vectors $\mathbf{k} = (\pm 1, 0, 0)$, $\mathbf{k} = (0, \pm 1, 0)$, \dots

This quantification of the permitted wave numbers has a consequence on the spatial forcing by the 3D torus $\hat{H}_0^{\text{T}}(\mathbf{k})$ or by a Dirac ring $\hat{H}_0^{\text{RD}}(\mathbf{k})$. On the one hand, in Figs. 16(a) and 16(c) we have plotted the theoretical forcing of $\hat{H}_0^{\text{T}}(\mathbf{k})$ and $\hat{H}_0^{\text{RD}}(\mathbf{k})$, based on formulas (A2) and (A1), respectively, with a continuous description of the wave vectors in terms of the modulus $k = |\mathbf{k}|$ and the angle θ . On the other hand, Figs. 16(b) and 16(d) show the numerical forcing $\hat{H}_0^{\text{T}}(\mathbf{k})$ and $\hat{H}_0^{\text{RD}}(\mathbf{k})$ based on the values of the wave vector in terms of modulus and angle discretized on the Cartesian grid such that $\mathbf{k} = (l, m, n)$, $(l, m, n) \in \{1, \dots, N_x\}^3$ with N_x the simulation resolution. When comparing the filters, the main difference between a continuous and a quantified grid comes from the large scales. Compared with the theoretical formulas for the two configurations, the energy contained in the small scales ($k > 30$) is well evaluated by the Cartesian grid, but the energy contained in the large scales is underestimated, with energy gaps at several θ angles. This numerical effect is more detrimental to the 3D torus configuration than to the Dirac ring configuration. Indeed, at fixed θ , compared to the theoretical formula, in the Dirac ring configuration the energy of the small scales is of the same order of magnitude as the energy of the large scales, which compensates for the gaps. However, this is no longer the case in the 3D torus configuration, as the larger scales contain noticeably more energy and the smaller scales can no longer compensate for the gaps. For each angle, the total energies injected by the forcing terms $\hat{H}_0^{\text{T}}(\mathbf{k})$ and $\hat{H}_0^{\text{RD}}(\mathbf{k})$ therefore vary between the theoretical formula and the Cartesian grid, but these variations are less significant for the ring of the Dirac configuration than for the 3D torus configuration. This has consequences for the vertical component of the velocity and the dissipation. Again, this phenomenon is observed equivalently in experiment and simulations whenever an enclosed fluid domain is considered.

APPENDIX C: FREQUENCY QUANTIZATION DUE TO THE SOURCE GEOMETRY

Figure 17(a) shows the distribution in the (θ, ω) plane of $E^{\text{L,NL}}(\theta, k, \omega)$ normalized by $E_{\text{tot}}^{\text{L,NL}}$ for $k = 12$ for nonlinear simulations in the torus configuration. The spectrum appears as concentrated energy along stripes, but the presence of the dispersion relation of IWs is clear. The stripes appear for two reasons:

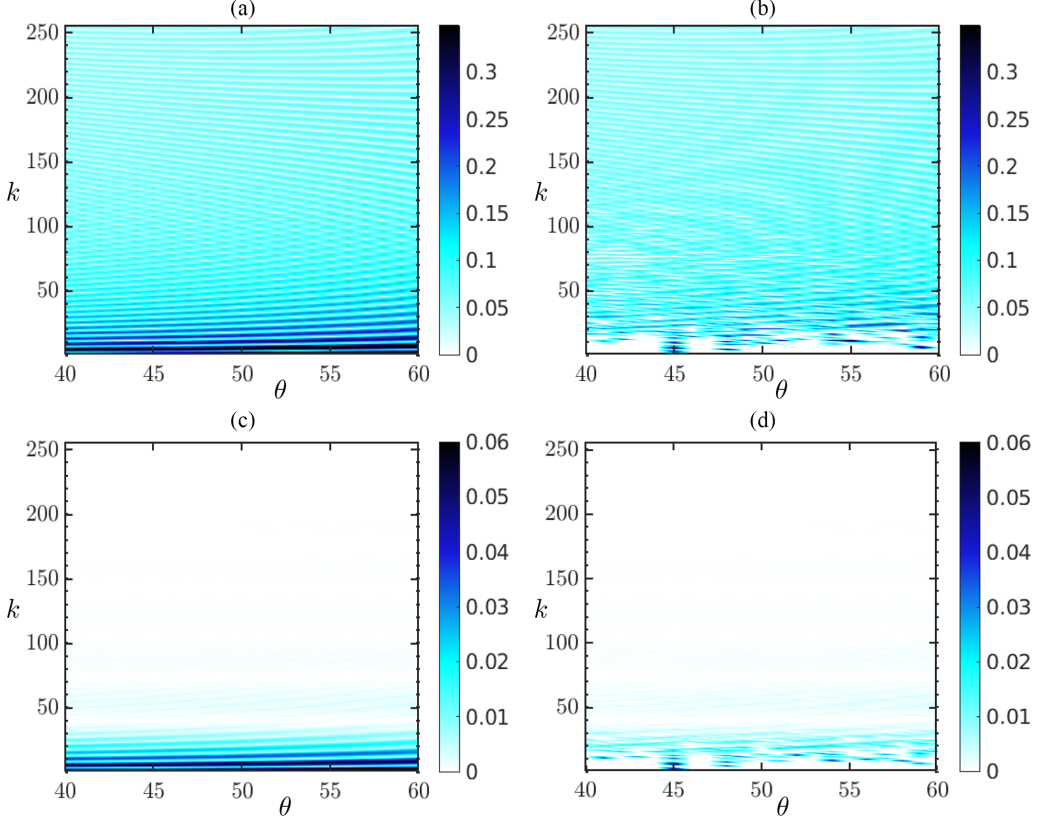


FIG. 16. Comparison of the modulus of the forcing of Dirac ring $|\widehat{H}_0^{\text{RD}}(k, \theta)|$ as a function of wave number k and the angle θ in the same range used in the simulations between (a) theoretical value from (A1) and (b) numerical computation from a Cartesian grid. The same is for for 3D torus forcing $|\widehat{H}_0^{\text{T}}(k, \theta)|$ between (c) theoretical values from Eq. (A2) and (d) numerical results.

(1) The quantization of the wave vectors since not all angles θ are possible due to the discretization on a Cartesian grid and bounded domain in particular at large scale (see Sec. IV B and Appendix B).

(2) The spatial forcing of the torus. Upon defining the average $\widehat{H}_0^{\text{T}}(k_0, \theta_0) = \sum_{|\mathbf{k}|=k_0, \theta(\mathbf{k})=\theta_0} \widehat{H}_0^{\text{T}}(k, \theta(\mathbf{k}))$ over all \mathbf{k} of norm k_0 and angle θ_0 , we observe that the forcing term $\widehat{H}_0^{\text{T}}(k_0 = 12, \theta_0)$ is zero for several angles θ visible in Fig. 17(a), which is due to the Cartesian grid.

At fixed k , we compute the number $N(k, \theta)$ of possible points on the grid for each θ_0 . Figure 17(b) shows these two sources of stripes, $\widehat{H}_0^{\text{T}}(k_0, \theta_0)$ and $N(k, \theta)$, normalized, respectively, by $\max_{\theta} (\widehat{H}_0^{\text{T}}(k = 1, \theta))$ and $\sum_{\theta} (N(k = 12, \theta))$. Moreover, the product of the two sources of stripes $\widehat{H}_0^{\text{T}}(k_0, \theta_0)N(k_0, \theta_0)$ is also plotted in the figure to identify the angles that form the stripes, based on the two previous reasons. The figure shows the coincidence of the zeros and variations of this function of kinetic energy density with the modulation with θ plotted in Fig. 17(a).

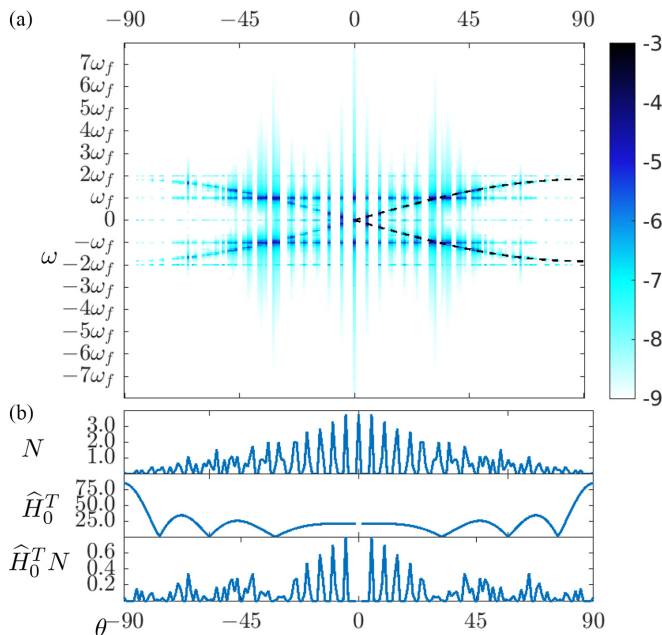


FIG. 17. (a) Angular spectral kinetic energy density $E^{\text{NL}}(\theta, k_0 = 12, \omega)/E_{\text{tot}}^{\text{NL}}$ for $\theta_f = 33^\circ$. The dashed black lines represent the dispersion relation $\omega_{dr}(\theta)$ defined in Eq. (1). The color bar indicates the log of the amplitude. (b) Dependence on θ of $\widehat{H}_0^T(k = 12, \theta)$ normalized by $\max(\widehat{H}_0^T(k = 1, \theta))$ (middle panel), and $N(k = 12, \theta)$ normalized by $\sum_{\theta} N(k = 12, \theta)$ (top panel), $\widehat{H}_0^T(k = 12, \theta)N(k = 12, \theta)$, plotted in percentage to indicate the injected power in different stripes.

-
- [1] K. Aldridge and L. Lumb, Inertial waves identified in the Earth's fluid outer core, *Nature (London)* **325**, 421 (1987).
- [2] J. Pedlosky, *Geophysical Fluid Dynamics* (Springer Science & Business Media, New York, 2013).
- [3] S. A. Thorpe, *An Introduction to Ocean Turbulence* (Cambridge University Press, Cambridge, 2007).
- [4] J. MacKinnon, Mountain waves in the deep ocean, *Nature (London)* **501**, 321 (2013).
- [5] J. M. Klymak, S. Legg, M. H. Alford, M. Buijsman, R. Pinkel, and J. D. Nash, The direct breaking of internal waves at steep topography, *Oceanography* **25**, 150 (2012).
- [6] V. Vlasenko, N. Stashchuk, M. E. Inall, M. Porter, and D. Aleynik, Focusing of baroclinic tidal energy in a canyon, *J. Geophys. Res.: Oceans* **121**, 2824 (2016).
- [7] M. C. Buijsman, J. M. Klymak, S. Legg, M. H. Alford, D. Farmer, J. A. MacKinnon, J. D. Nash, J.-H. Park, A. Pickering, and H. Simmons, Three-dimensional double-ridge internal tide resonance in Luzon Strait, *J. Phys. Oceanogr.* **44**, 850 (2014).
- [8] A. Peliz, B. Le Cann, and C. Mohn, Circulation and mixing in a deep submerged crater: Tore seamont, *Geophys. Res. Abs.* **11**, 7567 (2009).
- [9] J. Appleby and D. Crighton, Internal gravity waves generated by oscillations of a sphere, *J. Fluid Mech.* **183**, 439 (1987).
- [10] R. Bardakov, A. Y. Vasil'Ev, and Y. D. Chashechkin, Calculation and measurement of conical beams of three-dimensional periodic internal waves excited by a vertically oscillating piston, *Fluid Dyn.* **42**, 612 (2007).
- [11] S. Le Dizès, Wave field and zonal flow of a librating disk, *J. Fluid Mech.* **782**, 178 (2015).
- [12] S. Le Dizès and M. Le Bars, Internal shear layers from librating objects, *J. Fluid Mech.* **826**, 653 (2017).

- [13] Y. Duguet, J. F. Scott, and L. Le Penven, Oscillatory jets and instabilities in a rotating cylinder, *Phys. Fluids* **18**, 104104 (2006).
- [14] O. Bühler and C. J. Muller, Instability and focusing of internal tides in the deep ocean, *J. Fluid Mech.* **588**, 1 (2007).
- [15] N. Grisouard and O. Bühler, Forcing of oceanic mean flows by dissipating internal tides, *J. Fluid Mech.* **708**, 250 (2012).
- [16] E. V. Ermanyuk, N. Shmakova, and J.-B. Flór, Internal wave focusing by a horizontally oscillating torus, *J. Fluid Mech.* **813**, 695 (2017).
- [17] P. Maurer, S. Ghaemsaidi, S. Joubaud, T. Peacock, and P. Odier, An axisymmetric inertia-gravity wave generator, *Exp. Fluids* **58**, 143 (2017).
- [18] M. Duran-Matute, J.-B. Flór, F. S. Godeferd, and C. Jause-Labert, Turbulence and columnar vortex formation through inertial-wave focusing, *Phys. Rev. E* **87**, 041001(R) (2013).
- [19] N. D. Shmakova and J.-B. Flór, Nonlinear aspects of focusing internal waves, *J. Fluid Mech.* **862**, R4 (2019).
- [20] N. Shmakova, B. Voisin, J. Sommeria, and J.-B. Flór, Internal and inertia-gravity wave focusing at large Stokes numbers, *Phys. Rev. Fluids* **6**, 114804 (2021).
- [21] P.-Y. Passaggia, V. K. Chalamalla, M. W. Hurley, A. Scotti, and E. Santilli, Estimating pressure and internal-wave flux from laboratory experiments in focusing internal waves, *Exp. Fluids* **61**, 238 (2020).
- [22] B. Voisin, Internal wave focusing by annular forcing, in *International Symposium on Stratified Flows* (University of San Diego, 2016), Vol. 1.
- [23] J. Liu, M. Oberlack, Y. Wang, A. Delache, and F. S. Godeferd, Focusing of inertial waves by a vertically annular forcing, *Phys. Fluids* **34**, 086601 (2022).
- [24] H. P. Greenspan, *The Theory of Rotating Fluids* (Cambridge University Press, 1969).
- [25] B. Voisin, E. Ermanyuk, and J. Flór, Internal wave generation by oscillation of a sphere, with application to internal tides, *J. Fluid Mech.* **666**, 308 (2011).
- [26] T. Dauxois, S. Joubaud, P. Odier, and A. Venaille, Instabilities of internal gravity wave beams, *Annu. Rev. Fluid Mech.* **50**, 131 (2018).
- [27] D. Kolomenskiy and K. Schneider, A Fourier spectral method for the Navier–Stokes equations with volume penalization for moving solid obstacles, *J. Comput. Phys.* **228**, 5687 (2009).
- [28] C. Jause-Labert, F. S. Godeferd, and B. Favier, Numerical validation of the volume penalization method in three-dimensional pseudo-spectral simulations, *Comput. Fluids* **67**, 41 (2012).
- [29] E. Arquis and J. Caltagirone, Sur les conditions hydrodynamiques au voisinage d’une interface milieu fluide-milieu poreux: Application à la convection naturelle, *C. R. Acad. Sci. Paris II* **299**, 1 (1984).
- [30] P. Angot, C. Bruneau, and P. Fabrie, A penalization method to take into account obstacles in incompressible viscous flows, *Numer. Math.* **81**, 497 (1999).
- [31] C. Jause Labert, Simulation numérique d’écoulements turbulents en rotation, confinement et forçage à l’aide d’une méthode de pénalisation, Ph.D. thesis, Ecole Centrale de Lyon, 2012, <https://theses.hal.science/tel-00783702>.
- [32] E. W. Hester, G. M. Vasil, and K. J. Burns, Improving accuracy of volume penalised fluid-solid interactions, *J. Comput. Phys.* **430**, 110043 (2021).
- [33] F. S. Godeferd and F. Moisy, Structure and dynamics of rotating turbulence: A review of recent experimental and numerical results, *Appl. Mech. Rev.* **67**, 030802 (2015).
- [34] D. J. Bodony, Analysis of sponge zones for computational fluid mechanics, *J. Comput. Phys.* **212**, 681 (2006).
- [35] R. Kerswell, On the internal shear layers spawned by the critical regions in oscillatory Ekman boundary layers, *J. Fluid Mech.* **298**, 311 (1995).
- [36] P.-P. Cortet, C. Lamriben, and F. Moisy, Viscous spreading of an inertial wave beam in a rotating fluid, *Phys. Fluids* **22**, 086603 (2010).
- [37] N. Machicoane, P.-P. Cortet, B. Voisin, and F. Moisy, Influence of the multipole order of the source on the decay of an inertial wave beam in a rotating fluid, *Phys. Fluids* **27**, 066602 (2015).

- [38] P. A. Davidson, *Turbulence in Rotating, Stratified and Electrically Conducting Fluids* (Cambridge University Press, 2013).
- [39] H. Greenspan, On the non-linear interaction of inertial modes, *J. Fluid Mech.* **36**, 257 (1969).
- [40] M. Brunet, B. Gallet, and P.-P. Cortet, Shortcut to geostrophy in wave-driven rotating turbulence: The quartet instability, *Phys. Rev. Lett.* **124**, 124501 (2020).
- [41] S. Boury, I. Sibgatullin, E. Ermanyuk, N. Shmakova, P. Odier, S. Joubaud, L. Maas, and T. Dauxois, Vortex cluster arising from an axisymmetric inertial wave attractor, *J. Fluid Mech.* **926**, A12 (2021).
- [42] T. Le Reun, B. Favier, and M. Le Bars, Experimental study of the nonlinear saturation of the elliptical instability: Inertial wave turbulence versus geostrophic turbulence, *J. Fluid Mech.* **879**, 296 (2019).
- [43] P. Davidson, P. Staplehurst, and S. Dalziel, On the evolution of eddies in a rapidly rotating system, *J. Fluid Mech.* **557**, 135 (2006).
- [44] A. Ranjan and P. Davidson, Evolution of a turbulent cloud under rotation, *J. Fluid Mech.* **756**, 488 (2014).
- [45] A. C. Newell, Rossby wave packet interactions, *J. Fluid Mech.* **35**, 255 (1969).
- [46] T. Le Reun, B. Gallet, B. Favier, and M. Le Bars, Near-resonant instability of geostrophic modes: Beyond Greenspan's theorem, *J. Fluid Mech.* **900**, R2 (2020).
- [47] L. M. Smith and F. Waleffe, Transfer of energy to two-dimensional large scales in forced, rotating three-dimensional turbulence, *Phys. Fluids* **11**, 1608 (1999).
- [48] H. Lam, A. Delache, and F. Godefert, Supply mechanisms of the geostrophic mode in rotating turbulence: Interactions with self, waves and eddies, *J. Fluid Mech.* **971**, A10 (2023).
- [49] F. Beckebanze, K. Raja, and L. Maas, Mean flow generation by three-dimensional nonlinear internal wave beams, *J. Fluid Mech.* **864**, 303 (2019).
- [50] L. Biferale, S. Musacchio, and F. Toschi, Inverse energy cascade in three-dimensional isotropic turbulence, *Phys. Rev. Lett.* **108**, 164501 (2012).
- [51] F. Plunian, A. Teimurazov, R. Stepanov, and M. K. Verma, Inverse cascade of energy in helical turbulence, *J. Fluid Mech.* **895**, A13 (2020).
- [52] W. Agoua, B. Favier, A. Delache, A. Briard, and W. J. T. Bos, Spontaneous generation and reversal of helicity in anisotropic turbulence, *Phys. Rev. E* **103**, L061101 (2021).
- [53] A. Maffioli, A. Delache, and F. S. Godefert, Signature and energetics of internal gravity waves in stratified turbulence, *Phys. Rev. Fluids* **5**, 114802 (2020).
- [54] K. Dohan and B. Sutherland, Internal waves generated from a turbulent mixed region, *Phys. Fluids* **15**, 488 (2003).
- [55] S. Boury, P. Maurer, S. Joubaud, T. Peacock, and P. Odier, Triadic resonant instability in confined and unconfined axisymmetric geometries, *J. Fluid Mech.* **957**, A20 (2023).
- [56] E. Yarom and E. Sharon, Experimental observation of steady inertial wave turbulence in deep rotating flows, *Nat. Phys.* **10**, 510 (2014).
- [57] H. Lam, A. Delache, and F. S. Godefert, Partitioning waves and eddies in stably stratified turbulence, *Atmosphere* **11**, 420 (2020).
- [58] A. Campagne, B. Gallet, F. Moisy, and P.-P. Cortet, Disentangling inertial waves from eddy turbulence in a forced rotating-turbulence experiment, *Phys. Rev. E* **91**, 043016 (2015).
- [59] P. Clark di Leoni, P. J. Cobelli, and P. D. Mininni, The spatio-temporal spectrum of turbulent flows, *Eur. Phys. J. E* **38**, 136 (2015).
- [60] T. Le Reun, B. Favier, and M. Le Bars, Evidence of the Zakharov-Kolmogorov spectrum in numerical simulations of inertial wave turbulence, *Europhys. Lett.* **132**, 64002 (2020).
- [61] E. Monsalve, M. Brunet, B. Gallet, and P.-P. Cortet, Quantitative experimental observation of weak inertial-wave turbulence, *Phys. Rev. Lett.* **125**, 254502 (2020).
- [62] S. Galtier, *Physics of Wave Turbulence* (Cambridge University Press, 2022).
- [63] T. Le Reun, B. Favier, and M. Le Bars, Parametric instability and wave turbulence driven by tidal excitation of internal waves, *J. Fluid Mech.* **840**, 498 (2018).
- [64] C. Brouzet, Internal wave attractors: From geometrical focusing to non-linear energy cascade and mixing, Ph.D. thesis, Université de Lyon, 2016, <https://theses.hal.science/tel-01361201/>.

- [65] D. Oks, P. D. Mininni, R. Marino, and A. Pouquet, Inverse cascades and resonant triads in rotating and stratified turbulence, *Phys. Fluids* **29**, 111109 (2017).
- [66] A. Swami, J. M. Mendel, and C. L. Nikias, *Higher-Order Spectral Analysis Toolbox for Use with Matlab*, MathWorks Partner Series (Math Works, 1995).
- [67] P. Sagaut and C. Cambon, *Homogeneous Turbulence Dynamics* (Cambridge University Press, 2008).
- [68] M. Beleggia, M. De Graef, and Y. T. Millev, Magnetostatics of the uniformly polarized torus, *Proc. R. Soc. A* **465**, 3581 (2009).